Journal of Geosciences, 55 (2010), 347–368 DOI: 10.3190/jgeosci.082

Original paper

The nature of "quartz eyes" hosted by dykes associated with Au–Bi–As–Cu, Mo–Cu, and base-metal–Au–Ag mineral occurrences in the Mountain Freegold region (Dawson Range), Yukon, Canada

Thierry BINELI BETSI*, David R LENTZ

Department of Geology, University of New Brunswick, Fredericton, New Brunswick E3B5A3, Canada; thiery.bineli@unb.ca
** Corresponding author*

Various origins have been assigned to rounded to subrounded and elliptical quartz megacrysts ("quartz eyes") in dyke rocks associated with mineral deposits/occurrences worldwide. An exact interpretation of their nature is likely to tightly constrain the petrogenesis of the host rocks, and by association may be critical in evaluating genetic models for spatially associated ore minerals. ChromaSEM-CL imaging and electron probe microanalysis (EPMA) of "quartz eyes" within porphyry dykes associated with Au–Bi–Cu–As, Mo–Cu, and base-metal–Au–Ag mineral occurrences across the Northern Freegold Resources (NFR) property in the Dawson Range of Yukon Territory, Canada, reveals that the cathodoluminescence (CL) response of quartz is a function of its trace-element abundance(s). Bright blue luminescent growth zones are in most cases richer in Fe (up to 8839 ppm) and Ti (up to 229 ppm) relative to CL dark growth zones, with up to 41 times lower concentration of these elements. Assuming $^{a}TiO_2 = 1$, the Ti-poor dull cores consistently recorded lower temperatures (mostly < 600 °C) compared to Ti-rich brighter blue rims (up to 860 °C). This suggests either overgrowth on xenocrystic cores or an increase in crystallization temperature. The temperature rise likely reflects magma mixing, and is therefore consistent with the phenocryst/phenoclasts having formed in a magma chamber rather than by secondary processes. Also, the great variability in composition and temperature of crystallization and/or reequilibration of brighter blue growth zones of two quartz crystals (660 °C and 855 °C) from a single sample suggests that multiple episodes of magma mixing and incremental growth of parental magma chambers occurred. Some "quartz eyes" are overprinted by variably oriented, bifurcating, and anastomosing fluid migration trails ("splatter and cobweb textures") of red to reddish-brown CL quartz that is in most cases of low-temperature origin, and trace-elements poor, thus implying interaction of deuteric fluids with quartz phenocrysts/phenoclasts. The presence of "quartz eye" crystals with broken and angular blue cores, overgrown by oscillatory-zoned rims in which the zoning pattern does not correspond with the crystal boundaries, further suggests that some quartz crystals had been explosively fragmented (phenocrysts) and are now hosted in a recrystallized tuffisitic groundmass. The volatile exsolution that likely accompanied both magma mixing and decompression (as suggested by dendritic quartz, fine-grained recrystallized tuffisitic groundmass, and corroded quartz grains) was probably an important process that could have favoured the ore formation.

Keywords: scanning electron microscopy-cathodoluminescence, electron probe microanalysis, quartz eyes, Freegold Mountain, phenocryst, phenoclast, Yukon
Received: 18 August 2010; accepted: 21 December 2010; handling editor: S. Vrána

1. Introduction

Numerous deposits and mineral occurrences worldwide are associated with rounded to subrounded and elliptical quartz-bearing rocks and that quartz is usually referred to as "quartz eyes". Based on field observations alone, diverse genetic models have been assigned to these quartz crystals: (i) hydrothermal origin (Evans 1944), (ii) phenocrystic origin, i.e., high-T crystallization from a magma chamber (Vernon 1986), (iii) magmatic origin, but crystallized *in situ* at the intrusion level at *c.* 600 °C (magmatic hydrothermal transition), rather than in the subvolcanic magma chamber (see Müller et al. 2009 – usually referred to as "snowball quartz"), (iv) tectonic origin, i.e., fragments derived by disaggregation of early (pre- or early syntectonic) veins, or other quartz-rich bodies (Williams and Carmichael 1987). Variable approaches involving microanalytical techniques, such as scanning electron microscopy-cathodoluminescence (SEM-CL), electron probe microanalysis (EPMA), secondary ion mass spectrometry (SIMS), laser-ablation inductively coupled plasma mass spectrometry (LA-ICP-MS) as well as fluid and melt inclusions analysis have all been used to decipher the nature of quartz crystals. These studies were able to constrain the provenance of clastic quartz (Dennen 1967; Zinkernagel 1978), discriminate between quartz from igneous, metamorphic, and hydrothermal environments (Götze et al. 2001; Götze 2002; Monecke et al. 2002), and to establish a correlation between CL luminosity variation in quartz and its

trace-element composition (Watt et al. 1997; Müller et al. 2003a, b; Landtwing and Pettke 2005; Jacamon and Larsen 2009).

In the Mountain Freegold area, Yukon, Canada, the "quartz eye"-bearing rocks are high-level subvolcanic porphyritic dykes. Although recent studies (Harris et al. 2003, 2004; Vasyukova et al. 2008) proposed a combined magmatic and hydrothermal origin for "quartz eyes" found in porphyry Cu deposits, relating them to the magmatic hydrothermal transition stage, quartz from subvolcanic environments may represent either primary magmatic crystals, xenocrysts entrained during magma ascent (from the source region, wall rocks traversed during ascent, or other magmas if mixing occurred), or broken crystals (phenoclasts). In addition, Bineli Betsi and Lentz (in press) discriminated two types of "quartz eyes" (based on their physical shape) within dykes from the Mountain Freegold area and location descriptors. Some quartz eyes exhibit deformation features such as subgrains and undulatory extinction, whereas others do not. This suggests that "quartz eyes" within the Mountain Freegold Complex may have multiple origins. Therefore, an investigation of the nature of "quartz eyes" may help to further constrain the petrogenesis of the host porphyritic dykes. Because the Northern Freegold Resources (NFR) Mountain Freegold Project hosts numerous zones of mineralization that are all spatially associated with "quartz eye"-bearing dykes, an accurate interpretation of these quartz crystals is critical to evaluating models for ore genesis throughout the NFR property.

In this paper we present coupled ChromaSEM-CL and EPMA data in order to constrain the trace-element distribution in "quartz eyes" and its relation to cathodoluminescence responses, and to reveal the nature of "quartz eyes" found in porphyry dykes from the Freegold Mountain area. This methodology was motivated by the numerous advantages (high spatial resolution, good spectral resolution, etc.) of the electron probe for trace-element microanalysis (see Robinson et al. 1998). Some of quartz investigated exhibits narrow overgrowth zones, and in a combined EPMA, SIMS, LA ICP-MS, SEM-CL study, Müller et al. (2003a) found EPMA to be the most reliable *in situ* method for obtaining quantitative trace-element analyses from quartz with narrow (<20 μm) growth zoning due to the small sampling spot size (about 5 μm). Data obtained in the course of this study exhibit an unambiguous relationship between CL colour and trace-element abundance, which has been related directly to the temperature of quartz formation. These observations lead to significant insights on the origin of "quartz eyes" in dykes associated with mineralization across the NFR Mountain Freegold project and by association complement the petrogenetic model developed for these suites of porphyritic dykes.

2. Geological background

The Freegold Mountain Project (west central Yukon, Canada), in the Dawson Range Au–Cu–(Mo) Belt of the Tintina Au-Province, is host to several deposits and mineral occurrences, and each mineralized area is typified by a distinct style of mineralization. These include for example the Nucleus Au–Bi–As–Cu deposit, the Tinta base-metal Au–Ag deposit, the Stoddart Mo–Cu mineral occurrence (Bineli Betsi and Lentz 2009, in print; Bineli Betsi and Bennett 2010), and the Emmon Hill Au–Sb mineral occurrences (McInnes et al. 1988; Smuk 1999) (see Fig. 1). Mineralized areas are underlain by strongly deformed, locally mylonitic, metasedimentary and metaigneous schistose and gneissose rocks probably of Devonian to Mississippian and older ages of the pericratonic Yukon–Tanana Terrane, which represents a composite of geological units that were accreted to the North American continent during the early Mesozoic (Colpron et al. 2006). The Yukon–Tanana Terrane within the project area had been intruded by numerous plutonic bodies that in turn are crosscut by porphyritic dyke swarms , mostly oriented east–west, basaltic–andesitic to rhyolitic in composition, and of Middle (98–109 Ma) to Late Cretaceous (75–78 Ma) ages (Bineli Betsi and Bennett 2010).

These porphyritic dykes host up to 20 vol. % of quartz eyes (Fig. 2a) and there is a close spatial association between quartz-eye-bearing dykes and mineralization (Fig. 2b). Throughout the Freegold Mountain area, "quartz eyes" are set in a fine-grained groundmass and are of various morphologies including: (i) euhedral hexagonal crystals (Fig. 3a), (ii) rounded to subrounded grains (Fig. 3b), (iii) broken quartz grains (Fig. 3c), (iv) elliptic grains and (v) embayed grains (Figs 3d–e). In places, "quartz eyes" are either surrounded by an embayed (most probably resorption) rim (Fig. 3d) and/or mantled by either carbonate or amphibole (Fig. 3g).

3. Analytical procedures

"Quartz eyes" from dykes associated with numerous styles of mineralization across the NFR Mountain Freegold project have been investigated during the course of this study by both ChromaSEM-CL and EPMA. These include quartz eyes from: (i) Nucleus Au–Cu–Bi–As deposit, (ii) Tinta base-metal–Au–Ag deposit, (iii) Stoddart Mo–Cu mineral occurrence, (iv) Emmon Hill Au–Sb mineral occurrence, (v) Goldstar Cu–Fe–Au skarn mineral occurrence and (vi) a non-mineralized zone (TB 460).

ChromaSEM-CL imaging is very useful in examining cryptic textures in quartz (see Hayward 1998) and was carried out on carbon-coated polished thin sections with a JEOL 6400 SEM at the University of New Brunswick.

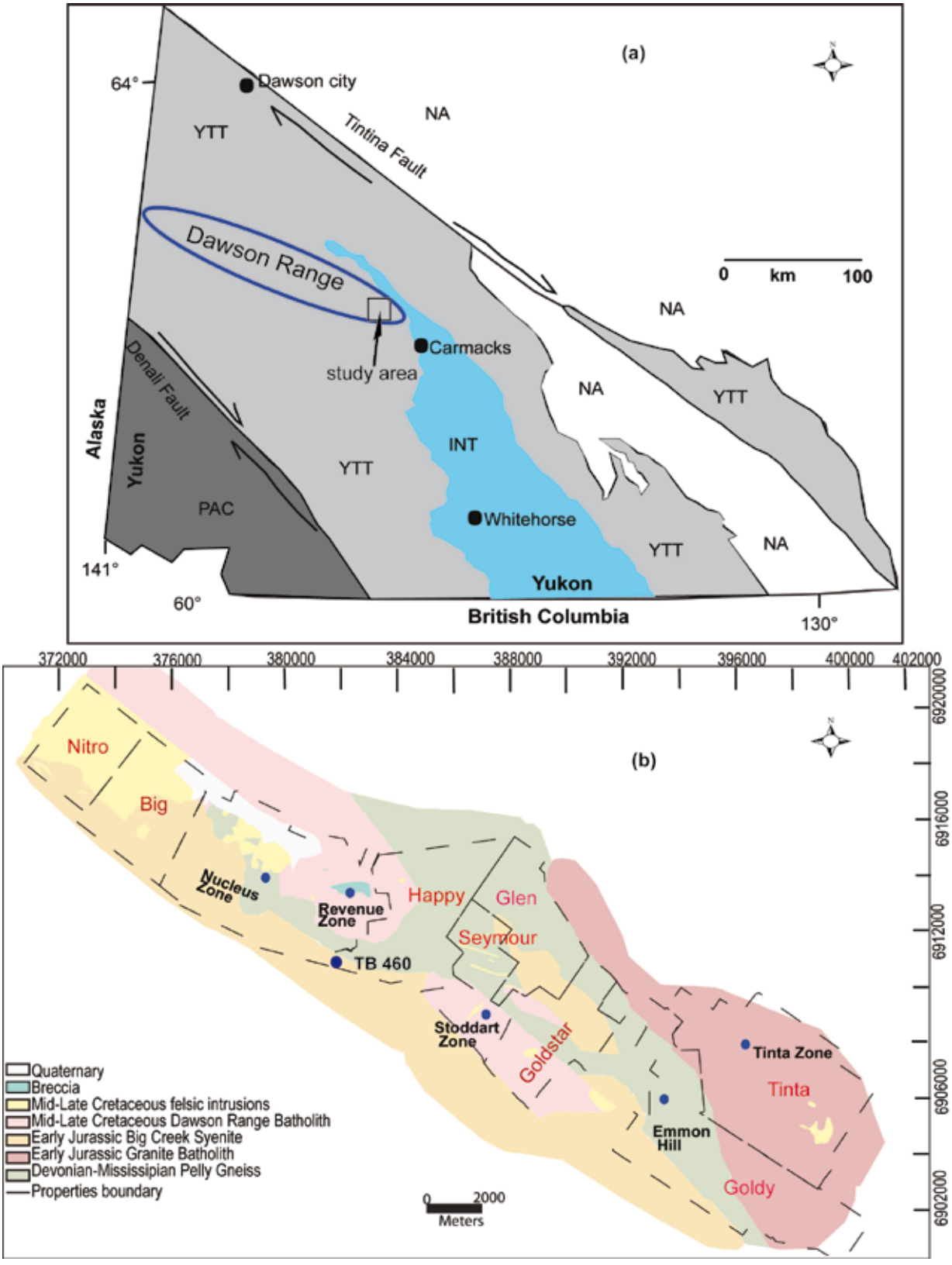

Fig. 1 (a) Simplified terrane map of the Yukon showing the Yukon–Tanana terrane, modified after Wheeler and McFeely (1991). NA, North America terrane; YTT, Yukon–Tanana terrane; INT, Intermontane Belt; PAC, Phanerozoic accreted crust. **(b)** Geology map from the study area (NFR Mountain Freegold property) also showing the location of Nucleus, Revenue, Goldstar, Stoddart, Emmon Hill, and Tinta Hill mineralized zones, Dawson Range, Yukon.

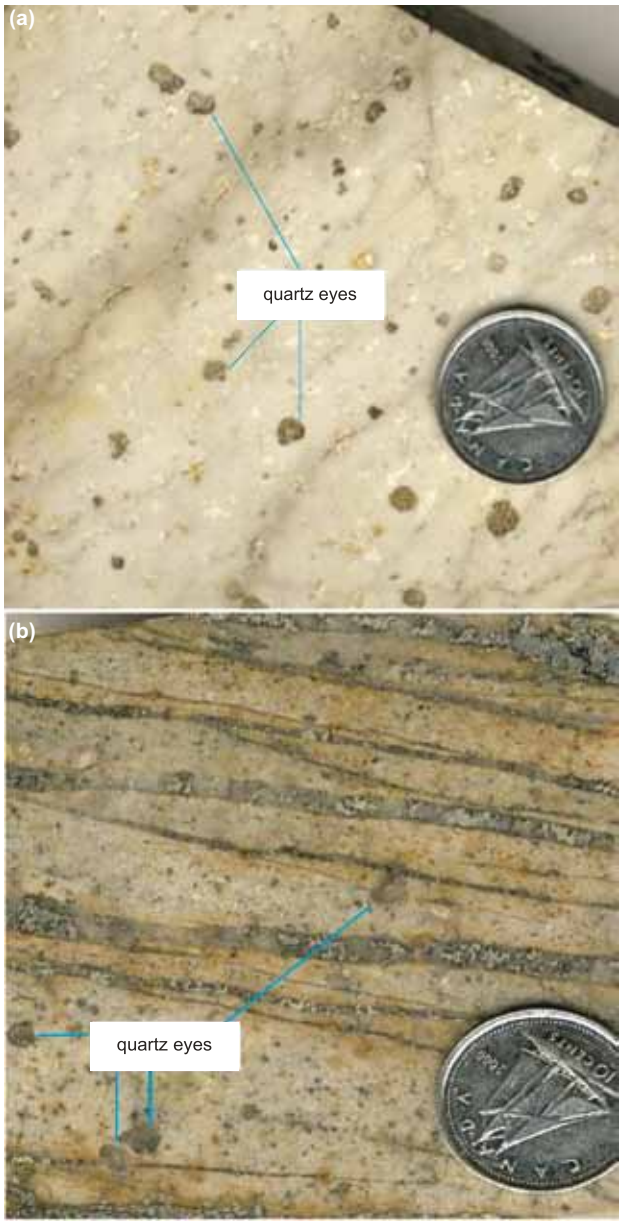

Fig. 2 Slab photographs of "quartz eye"-bearing dykes. **a** – Rhyolitic quartz–feldspar porphyry dyke (from Goldstar) exhibiting up to 20 vol. % "quartz eyes" (sample TB 254). **b** – "Quartz eyes"-bearing dyke from Nucleus hosting sheeted quartz–chalcopyrite–pyrite veins.

Back-scattered electron (BSE) and CL images were successively taken under the same analytical conditions (acceleration voltage of 15 kV and beam current of 10 nA) using a Gatan Chroma CL digital image acquisition system. The system used cannot quantify the CL intensity and only luminescence colours exhibited by quartz crystals were recorded. Scans in the region of each characteristic X-ray peak were acquired to ensure there were no interfering peaks. The analytical software uses a linear model to calculate the background contribution to the peak measurement. The concave curvature of the background in the region of the Al K_α and Na K_α peaks may result in a small underestimation of the background-corrected peak intensity.

Trace-element analyses of "quartz eyes" were acquired from carbon-coated polished thin sections, using a JEOL SUPERPROBE-733 electron-probe microanalyser, equipped with dQant32 and dsSpec automation from Geller Microanalytical Laboratories. An accelerating voltage of 25 kV and a probe current of 300 nA were used on quartz, and the counting times were 300 s on the peak, 150 s on the high, and 150 s on the low background. To account for the significant difference in characteristic X-ray intensities between the standards and the samples, the standard intensities were measured at a lower probe current (30 nA) than the sample intensities (300 nA) to avoid single-channel analyser (SCA) voltage pulse shift at high count rates. Detection limits are as follow: Na (25 ppm), Al (15 ppm), K (8 ppm), Ca (12 ppm), Ti (13 ppm), Mn (10 ppm), Fe (57 ppm), and Ge (66 ppm). Natural (jadeite, kaersutite, orthoclase, clinopyroxene, and bustamite) and synthetic ($SrTiO_3$, Fe metal 2, and Ge metal) standards were used. In each sample, zones of different cathodoluminescence colours were analyzed in order to relate the CL colour to the trace-element contents. Also some CL colour zones were analyzed on different points in order to evaluate the consistency of data.

4. ChromaSEM-CL responses

"Quartz eyes" investigated in the course of this study display numerous textures and CL colours. Textures observed across the different mineralized zones are variable (see Tab. 1) and include primary and secondary features. Primary textures typically consist of growth zones (single or multiple) and dendritic textures. Quartz crystals that exhibit a single growth zone (implying a single phase of crystallization) are either gray or gray-bluish coloured (Figs 4a–b). The presence of brighter spots within a single growth zone suggests a heterogeneous composition. Quartz with multiple growth zones is colour zoned and the zoning can be: (i) concentric, with dark euhedral to anhedral core overgrown by bright blue rim of variable thickness (Figs 5a–d), (ii) oscillatory, consisting of a heterogeneously coloured cores overgrown by alternating bands of dull and relatively brighter luminescent quartz (Figs 6a–f), (iii) patchy, where dark and relatively brighter zones are unevenly distributed both in the core and at the rims of the quartz crystals (Figs 7a–d). In places, the outer rims of quartz are overgrown by a thin (< 20 μm) layer of microcrystalline quartz, which displays a blue luminescence colour similar to quartz in the groundmass (Fig. 7b–d). Dendritic quartz is consistently of blue colour and occurs as either overgrowth on dark quartz or isolated crystals in the groundmass (Figs 8a–b). Den-

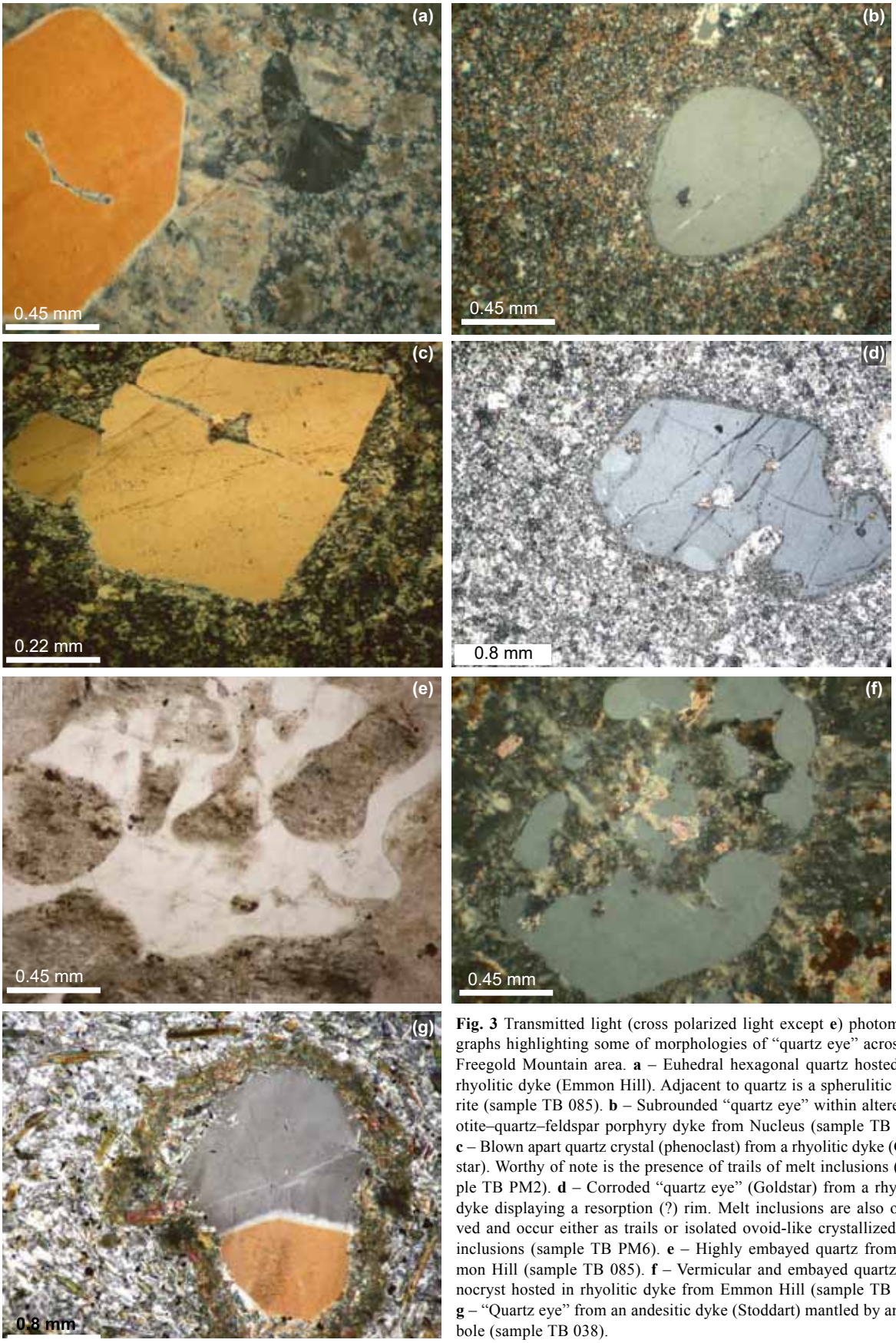

Fig. 3 Transmitted light (cross polarized light except **e**) photomicrographs highlighting some of morphologies of "quartz eye" across the Freegold Mountain area. **a** – Euhedral hexagonal quartz hosted in a rhyolitic dyke (Emmon Hill). Adjacent to quartz is a spherulitic chlorite (sample TB 085). **b** – Subrounded "quartz eye" within altered biotite–quartz–feldspar porphyry dyke from Nucleus (sample TB 407). **c** – Blown apart quartz crystal (phenoclast) from a rhyolitic dyke (Goldstar). Worthy of note is the presence of trails of melt inclusions (sample TB PM2). **d** – Corroded "quartz eye" (Goldstar) from a rhyolitic dyke displaying a resorption (?) rim. Melt inclusions are also observed and occur either as trails or isolated ovoid-like crystallized melt inclusions (sample TB PM6). **e** – Highly embayed quartz from Emmon Hill (sample TB 085). **f** – Vermicular and embayed quartz phenocryst hosted in rhyolitic dyke from Emmon Hill (sample TB 085). **g** – "Quartz eye" from an andesitic dyke (Stoddart) mantled by amphibole (sample TB 038).

Tab. 1 ChromaSEM-CL textures observed in mineralized zones across the NFR Freegold Mountain project

Mineralized zone	**CL textures**
Nucleus	Oscillatory and patchy zoning
Revenue	Splatter and cobweb textures
Tinta	Dendritic quartz, patchy and concentric zoning, and resorption and corrosion surfaces
Emmon Hill	Oscillatory and concentric zoning
Stoddart	Concentric zoning and resorption surfaces
Goldstar	Splatter and cobweb textures

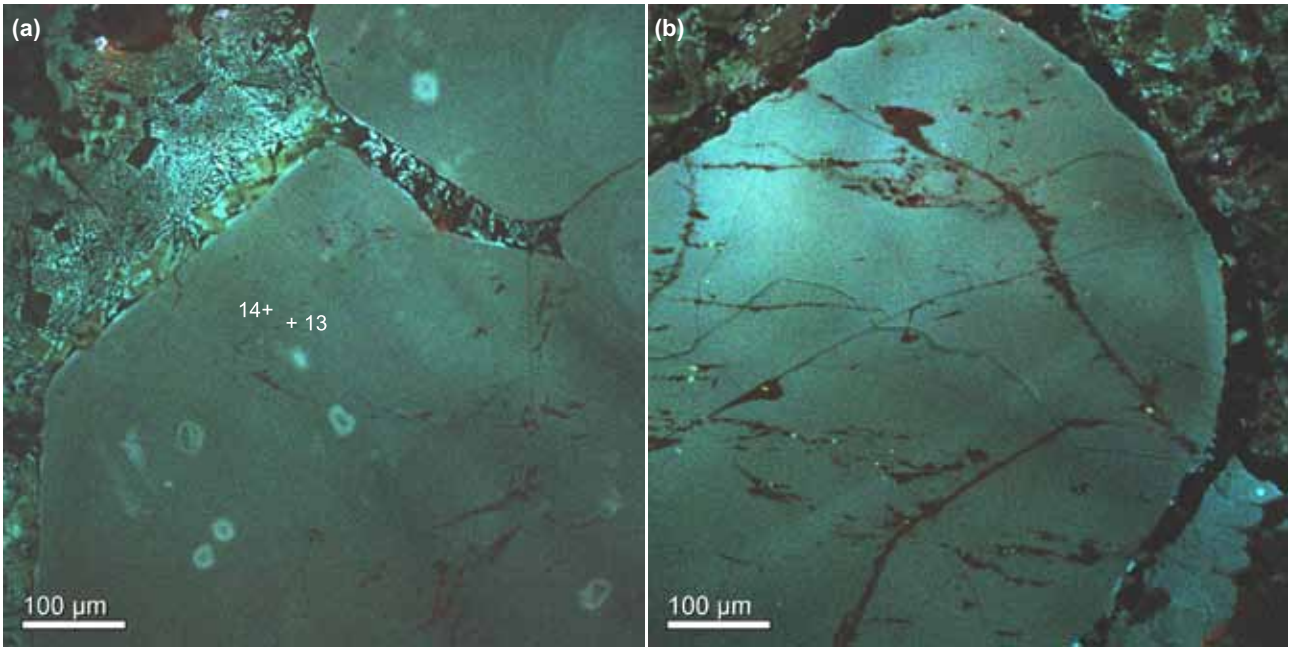

Fig. 4 ChromaSEM-CL images of some of primary textures exhibited by "quartz eyes" from the NFR Freegold Mountain project. **a –** Euhedral "quartz eye" hosted in a rhyolitic dyke (Emmon Hill) showing a single homogeneously CL dark-coloured growth zone, suggesting a single phase of crystallization, the bright spots are dust on the coated thin section (sample TB 085). **b** – Gray bluish quartz hosted in andesitic dyke from a non-mineralized zone (sample TB 460). The numbers in figures indicate the location of electron-microprobe spots.

dritic quartz is thought to develop with greater amounts of undercooling (at least 55 °C) caused by movement of magma to higher levels in the volcanic systems or by loss of volatiles (see Swanson and Fenn 1986).

Secondary textures involve "splatter" and "cobweb" textures, corrosion and resorption surfaces, and fragmentation features. "Splatter" and "cobweb" are overprinting textures that were observed in sugary aggregates of anhedral quartz crystals (type 2 quartz eyes of Bineli Betsi and Lentz, in press, from the Revenue Au–Cu occurrence and in "quartz eyes" associated with the Goldstar skarn mineral occurrence. The overprinting features occur as previously crystallized bluish quartz (quartz 1) invaded by variably oriented and anastomosing fluid migration trails in which new reddish to reddish-brown luminescent quartz (quartz 2) precipitated (Figs 9a–d). In places the newly crystallized reddish quartz cross cuts and surrounds earlier formed blue quartz (Fig. 9d). The resulting "splatter" and "cobweb" textures may be related to either quartz dissolution focused along fractures and microfractures, followed by precipitation of CL reddish-brown quartz into these newly created open spaces, or just quartz precipitation in already existing open fractures. Dissolution of quartz can result from heating of hydrothermal fluids, cooling of fluids through the zone of retrograde solubility of quartz (see Fournier 1999) or increase in pressure. Hydrothermal alteration or metamorphism may also explain the observed overprinting textures, and the causes of the CL contrast between fluid migration paths and the host quartz may be assigned to recrystallization and/or deformation processes caused by the diffusion and reaction of the fluids (Götze et al. 2001). The presence of subgrains in "quartz eyes" from Goldstar (sample TB PM3) invaded by later fluids may imply tectonic effects as well. "Splatter" and "cobweb" textures had been reported in hydrothermal quartz from porphyry copper and epithermal deposits

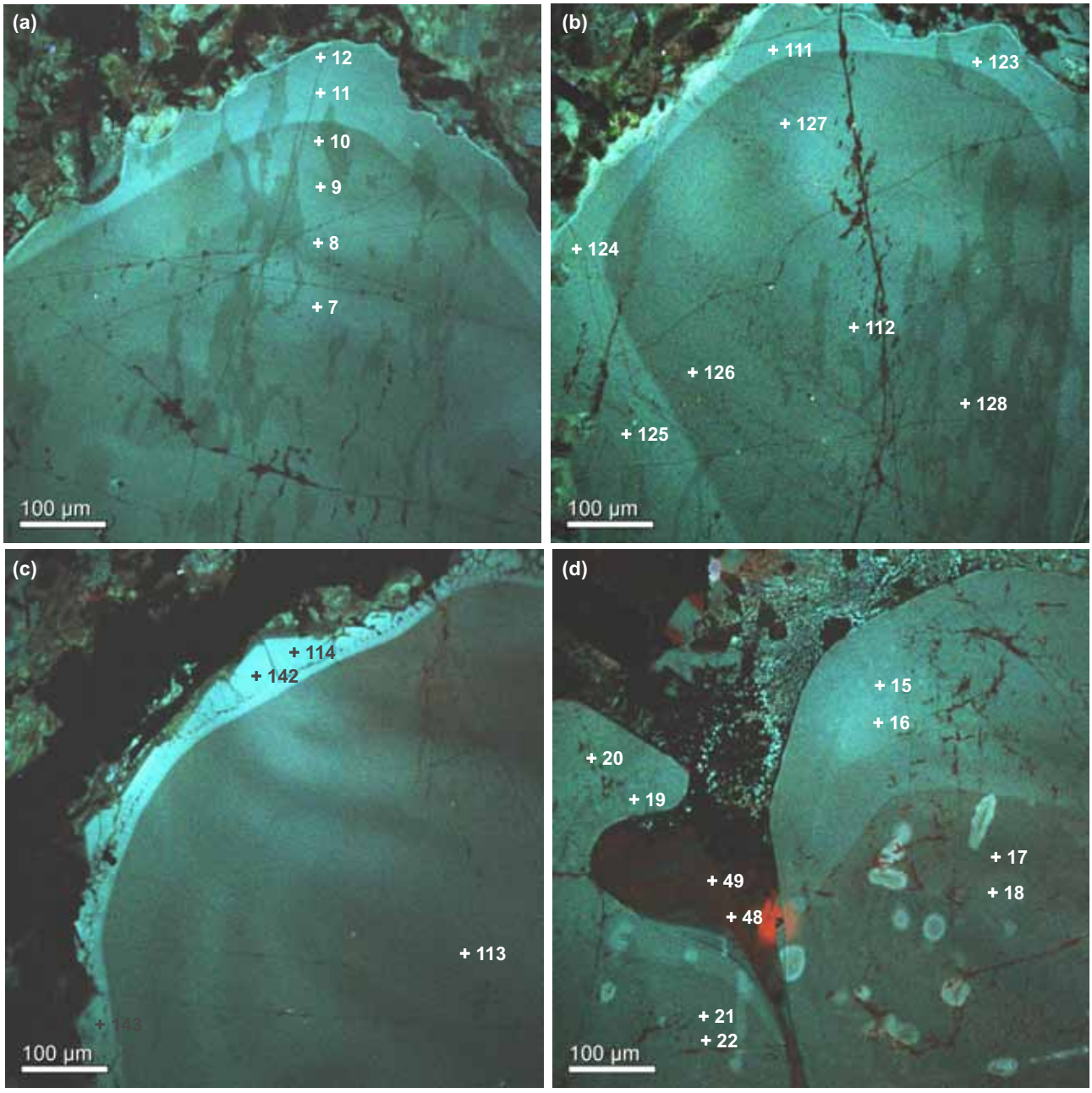

Fig. 5 ChromaSEM-CL images of quartz exhibiting dark core overgrown by lighter blue quartz. **a–c –** Quartz from andesitic dyke (Stoddard) displaying an anhedral dark core overgrown by blue zone (sample TB 038). **d –** Quartz from a rhyolitic dyke (Emmon Hill) showing a euhedral dark core overgrown by a lighter blue outer shell.

(Rusk et al. 2005), as well as in quartz from subvolcanic units worldwide, where they occur as dense networks of healed cracks with secondary quartz (van den Kerkhof et al. 2001; Müller et al. 2002a, 2005).

The ChromaSEM-CL response also allowed deciphering fragmental textures that were not observed through optical microscopy. Fragmented quartz consists of a broken and angular blue core overgrown by oscillatory-zoned rim wherein gray bands alternate with bands of brighter luminescing quartz (Fig. 6d). The observed zoning pattern of the rim does not correspond with the crystal boundaries (Fig. 6d), suggesting that even the newly overgrown zone (rim) had been thereafter explosively fragmented. This indicates the phenoclastic nature of this "quartz eye" type.

Corrosion results in the general rounding of quartz crystals as it can be seen, for example, in Figs 3b and 8b. Lobate embayed surfaces as observed in Figs 3d–e com-

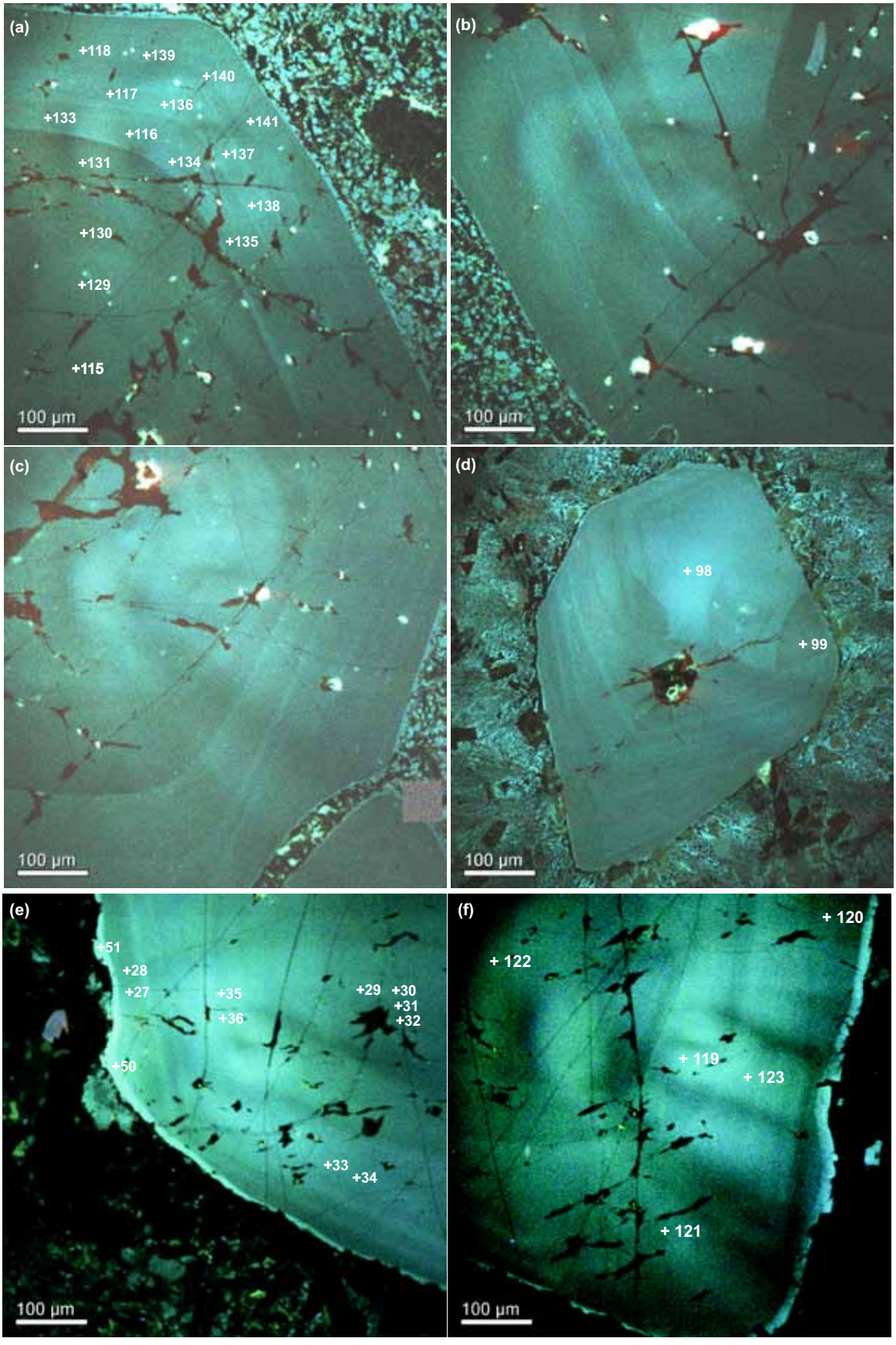
(a)
+118
+139
+140
+117
+136
+133
+141
+116
+131
+134
+137
+138
+130
+135
+129
+115
100 µm
(b)
100 µm
(c)
100 µm
(d)
+ 98
+ 99
100 µm
(e)
+51
+28
+27
+35
+29
+30
+31
+36
+32
+50
+33
+34
100 µm
(f)
+ 120
+ 122
+ 119
+ 123
+ 121
100 µm

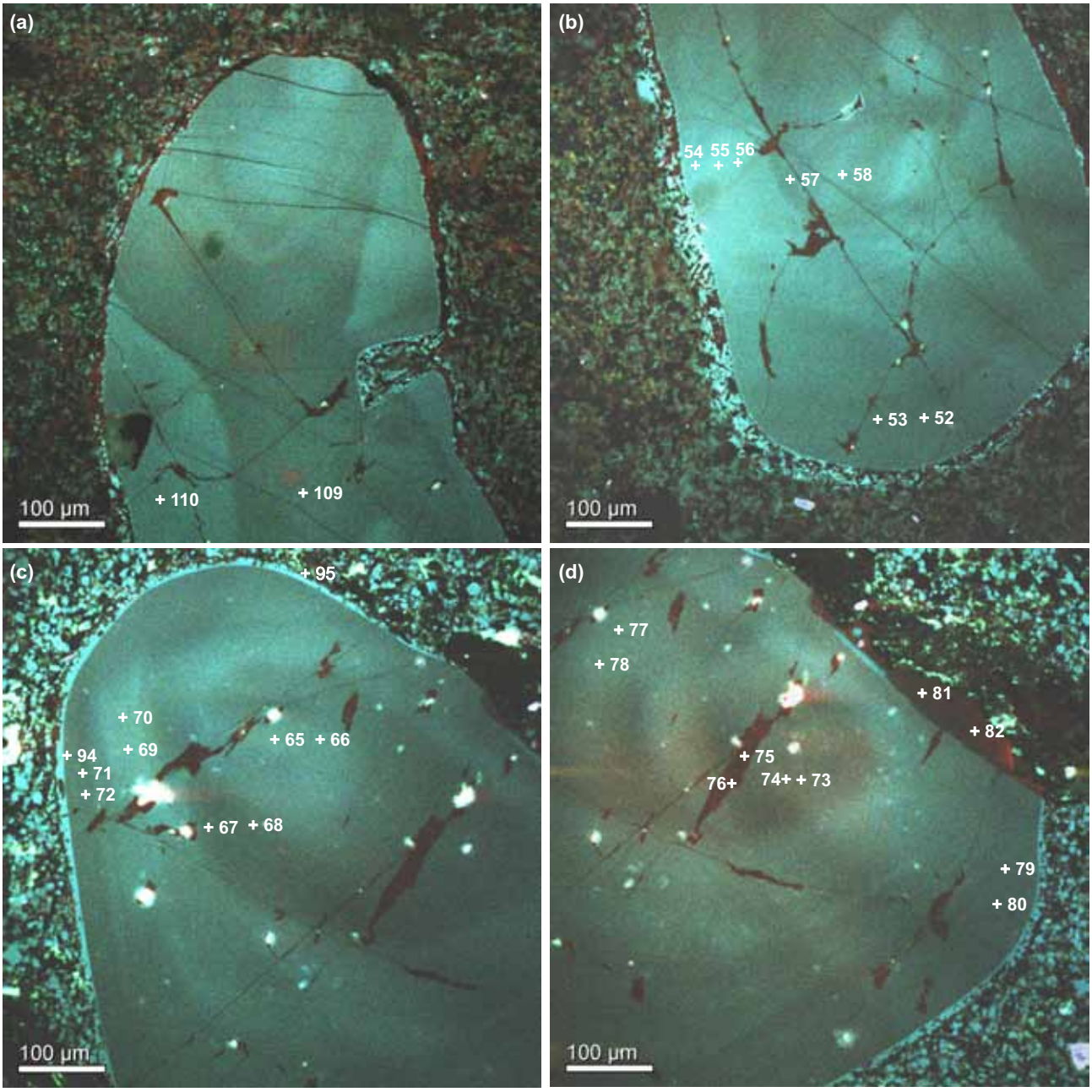

Fig. 7 ChromaSEM-CL images of patchy zoned quartz. **a–b** – Upper and basal portions, respectively, of quartz hosted in rhyolitic dyke (Nucleus). Both the core and the rim are patchy zoned with dark and light blue zones unevenly distributed through the core, which is overgrown by microcrystalline blue rim (sample TB 189). **c–d –** Quartz from a rhyolitic dyke (Nucleus) with patchy-zoned core overgrown by an oscillatory-zoned rim. The outer rims are in turn surrounded by a thin layer of blue microcrystalline quartz of a colour comparable to that of the quartz in the groundmass; the presence of red quartz is also noted (sample TB 323).

⇦

Fig. 6 ChromaSEM-CL images of quartz with oscillatory zoning. **a–c –** Quartz from a rhyolitic dyke (Nucleus) displaying a patchy zoned core overgrown by an oscillatory-zoned rim (sample TB 323). **d –** "Quartz eye" phenoclast hosted in rhyolitic dyke (Emmon Hill) displaying an angular and broken blue core overgrown by a rim comprised of alternating bands of blue and dark luminescent quartz. The zoning pattern of the rim does not correspond with the crystal boundaries (TB 085).

monly truncate pre-existing growth zones (Figs 8c–d), and they have therefore been interpreted as resorption surfaces, using the criteria adopted from Müller et al. (2003b). Both cores and rims of quartz are resorbed and resorption surfaces are of variable shape (wavy, rounded, and tooth-like). In most cases, resorption of the rim was followed by blue luminescent overgrowth of variable width (10–100 µm).

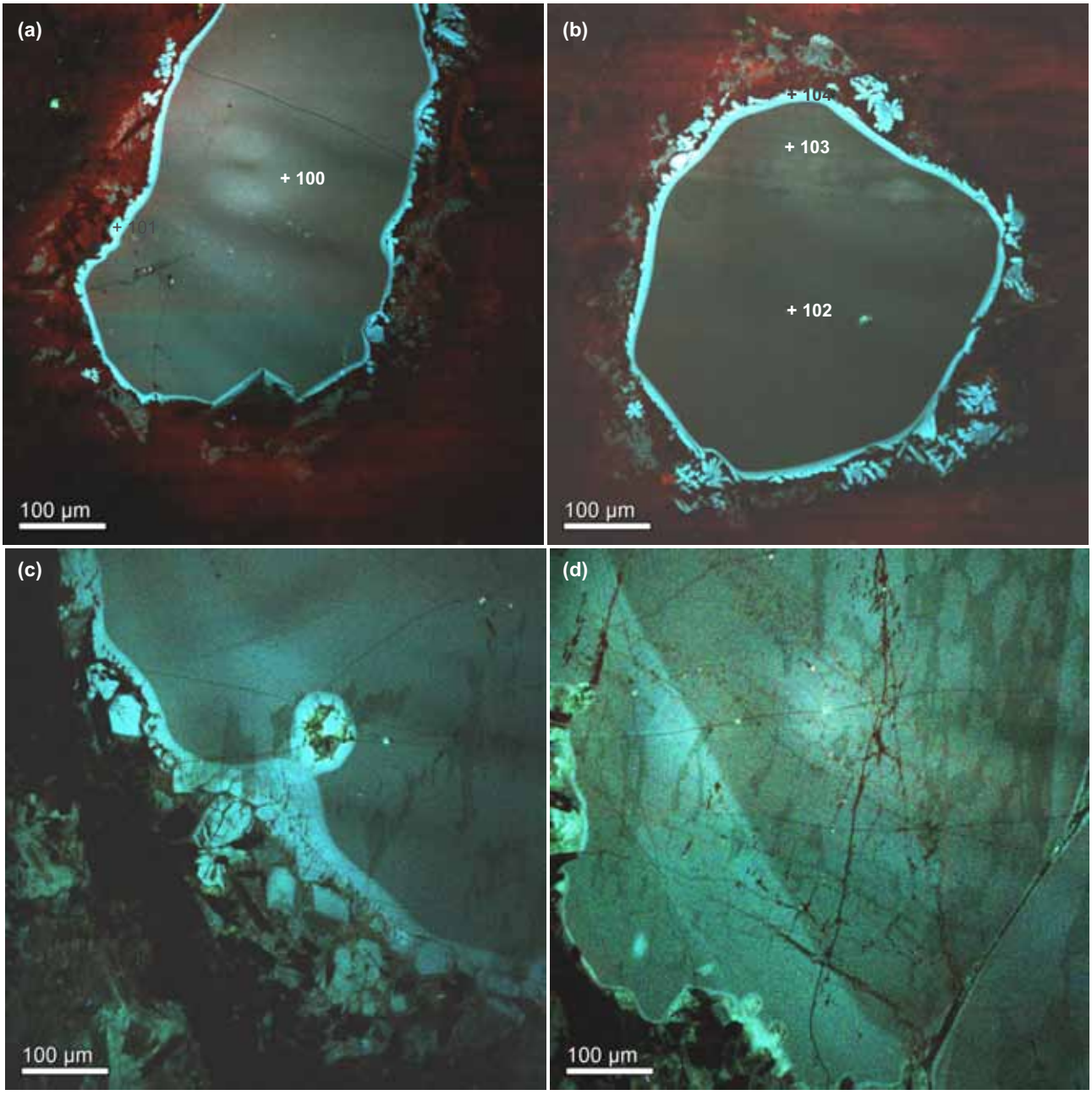

Fig. 8a–b – ChromaSEM-CL images of quartz from an altered chlorite-bearing trachytic dyke (Tinta) with a dark core overgrown by brighter blue luminescent dendritic quartz. Isolated dendritic quartz is additionally observed. The red mineral is calcite mantling the quartz crystals (sample TB 218). **c–d** – ChromaSEM-CL images of quartz from an andesitic dyke (Stoddart), where rims exhibit wavy resorbed surfaces (truncating previous growth zone), which in turn are overgrown by a thin (**c**) to very thin (**d**) layer of brighter quartz. Small euhedral quartz crystals likely to indicate devitrification texture are also observed. The ovoid-like blue spot in **c** is a crystallized melt inclusion suggesting that the latter was formed following partial resorption (sample TB 038).

Resorbed quartz grains also have melt inclusions that probably formed following partial resorption (Fig. 8c; see Lofgren 1980), rather than during skeletal growth usually taking place under high degree of undercooling (Roedder 1979; MacLellan and Trembath 1991). In addition, the ubiquity of euhedral small grains (Fig. 8c) may suggest vapour phase and devitrification textures.

5. Trace-element distribution

Only a few ions, such as Al^{3+}, Ti^{4+}, Ga^{3+}, Fe^{3+}, Ge^{4+} and P^{5+}, are likely to substitute for Si^{4+} in the quartz structure. Some of these require charge compensation by additional ions, such as Na^{+}, Ca^{2+}, Li^{+}, H^{+}, and K^{+} (see Müller and Koch–Müller 2009). Therefore, 143 spots in quartz from

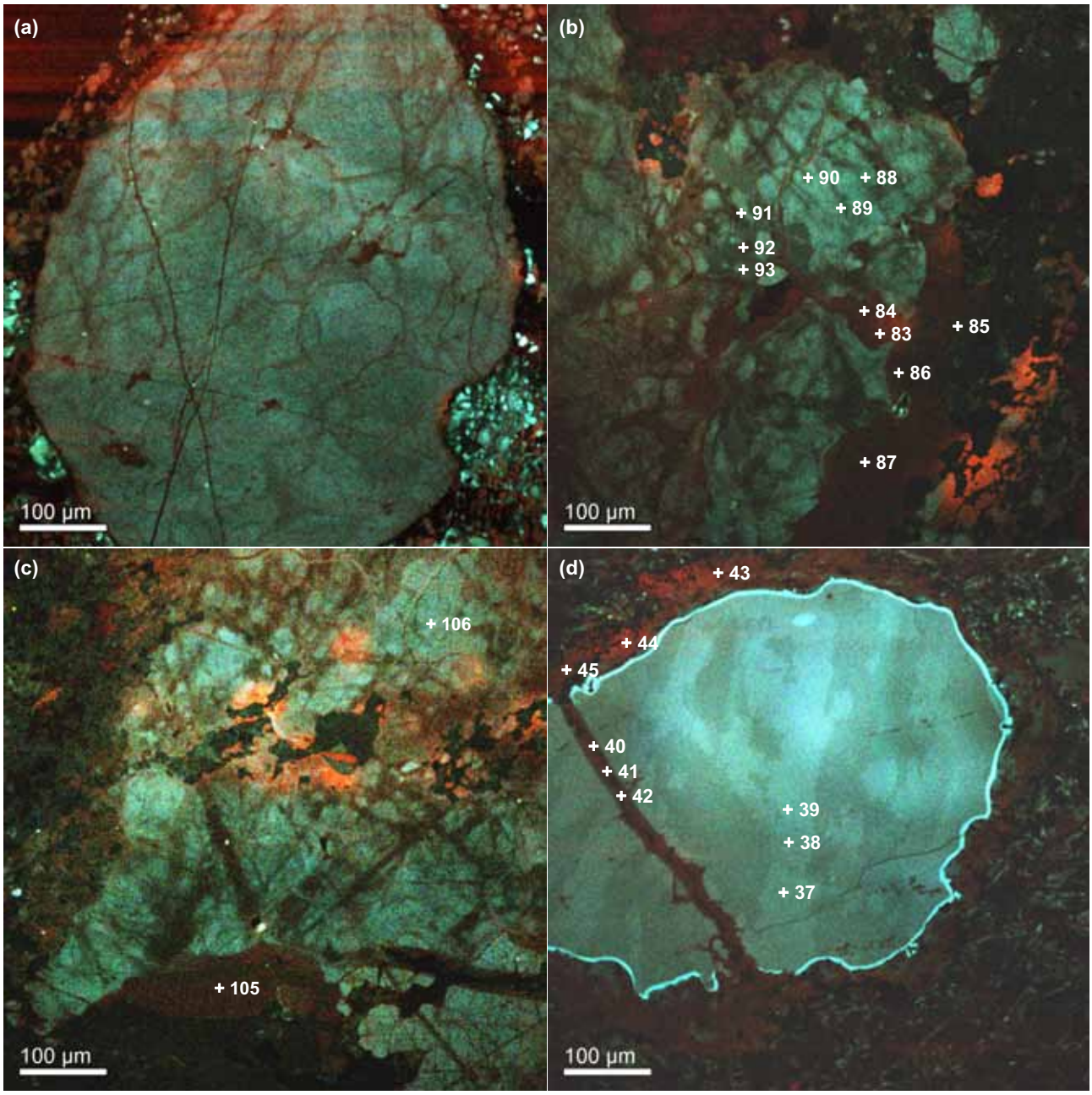

Fig. 9 ChromaSEM-CL example of overprinting textures observed in "quartz eyes" from the study area. **a –** Splatter and cobweb textures in an andesitic dyke from Goldstar consisting of variably oriented, anastomosing and bifurcating fractures and microfractures in which secondary brown reddish quartz precipitated (sample TB PM3). **b–c** – Splatter and cobweb textures in a rhyolitic dyke (from Revenue (sample TB 174). **d –** Resorbed dull quartz overgrown by a thin layer of bright blue quartz. This crystal from an andesitic dyke (Stoddart) is additionally crosscut by, and surrounded with, reddish quartz (sample TB 383).

13 "quartz eyes" crystals were analyzed for Al, Fe, Ti, Ge, Ca, Na, K, and Mn in the current study and results obtained are presented in Tab. 2. Aluminum is present in detectable concentrations in almost all (excepted two) analyzed spots and its abundance ranges from 36 to 6 311 ppm, thus showing that Al is the most important trace element in "quartz eyes" from the NFR Freegold Mountain project samples. This is typical of quartz from many geologic environments where Al is the most abundant trace element (Götze and Plötze 1997; Götze et al. 2004; Müller et al. 2005; Rusk et al. 2006). The Al content of quartz was not found to correlate with the peraluminosity of the melt as also reported by Breiter and Müller (2009).

Iron was not detected in many of analyzed spots, and where measured, its abundance varied between 84 and 8 839 ppm. Most of the elevated Fe abundances were observed to be associated with red quartz mantling bluish quartz (see Fig. 9d), as well as with bright blue luminescent overgrowth zone (Fig. 8a–b), which also recorded elevated Al abundance (about 4 000 ppm). Such elevated Fe abundance had been reported on stockwork quartz from the Grasberg porphyry-Cu–Au deposit (5 000 ppm, Penniston-Dorland 2001). Titanium concentrations were measured in the range from 16 up to 1 605 ppm. Titanium abundances greater than 229 ppm are typically associated with the red quartz mantling bluish quartz as referred earlier and such elevated Ti content is best explained by contamination from the groundmass. Sodium is essentially <25 ppm. However, Na abundances up to 433 ppm were reported in the red zones surrounding bluish quartz and that may once again be attributed to contamination from/reaction with the groundmass. Germanium and K contents are below the detection limits in most analyzed spots. Calcium is not detectable in many of analysis spots, but its abundance is abnormally elevated in places, where it is up to 2 750 ppm in the red quartz referred to above and up to 3 440 ppm in the blue overgrowth observed in Fig. 8a. Quartz in Figs 8a–b is mantled by carbonate (red CL colour) and thus elevated Ca content suggests infiltration from the surrounding carbonate.

Worthy of note is that the reddish-brown to red quartz from "splatter" and "cobweb" textures is either trace elements-depleted (apart from Al, which returned detectable abundance), thus consistent with previous studies showing that the secondary post-magmatic quartz is nearly trace-element free (van den Kerkhof et al. 2001; Müller et al. 2002b), or trace element-rich.

6. Discussion

6.1. Possible causes of the CL colour variations

In zoned quartz crystals from this study displaying dull and brighter blue growth zones, the highest abundances of Ti, Fe, and Ca are typically associated with blue overgrowths and bright zones (Tab. 2). Such a trend had been observed in numerous quartz pheno- and xenocrysts from volcanic rocks (Watt et al. 1997). Müller et al. (2003b) also reported high Ti content associated with blue luminescent growth zones in quartz phenocrysts from granite. Similar trace-element distribution is also noted in hydrothermal quartz from Bingham porphyry Cu–Au–Mo deposit where the highest concentrations of Al, Ti, K, and Na are recorded in bright luminescent quartz, whereas dark luminescent quartz exhibits the lowest contents (cf. Landtwing and Pettke 2005). By contrast the highest Al abundance was recorded in a dark core. This was also reported in hydrothermal vein quartz from the Butte Montana porphyry-copper where the highest concentration of Al has been observed to be associated with dull luminescing zones (Rusk et al. 2006). Therefore, variation in CL intensity and colour in natural quartz is unclear and has been related to various elements in the literature: Mn (Marshall 1988), Al (Grant and White 1978; Demars et al. 1996; Watt et al. 1997), monovalent cations Li, Na, and H (Penny et al. 1992; Demars et al. 1996; Ramseyer and Mullis 1990), Fe (Kempe et al. 1999), Ti (Müller et al. 2003; Rusk et al. 2006), Ge (Götze et al. 2004), H complexes (Fisher 2003), total trace-element concentration (Landtwing and Pettke 2005) and various crystal lattice defects, such as non-bridging oxygen hole centres (Götze et al. 2001).

In investigated quartz samples with clearly defined dark core and blue rims (as those illustrated in Figs 5 and 8), the highest Al content is observed to be associated with the dull domains if we exclude the blue rim that yielded abnormally elevated Al content (see Fig. 10a). Contrary to this, elevated Ti concentration is broadly associated with brighter blue zones (see Fig. 10b). Likewise, in quartz crystals exhibiting dark and brighter zones (such as observed in Figs 6 and 7), dark zones recorded the highest Al content (up to 738 ppm, see Tab. 2), whereas the higher Ti values are consistently associated with brighter zones. This is in disagreement with the observations of Demars et al. (1996) and Watt et al. (1997), where Al had been considered as the blue CL activator. Therefore it is reasonable to conclude that Ti is the blue CL luminescence activator in "quartz eyes" from the intrusive rocks across the NFR Freegold Mountain project. This is in agreement with the observation of Rusk et al. (2006), where Ti abundance was recognized to control the CL intensity.

6.2. Origin of quartz eyes

Variability in luminescence colours and in CL emission bands can result from intrinsic defects, which includes translational errors, points defects, inclusions of mineral, gas or liquid (Götze et al. 2001), as well as from external defects (incorporation of lattice-bound trace-elements). The defects causing different CL emissions often reflect the specific physico-chemical conditions of crystal growth and therefore can be used to investigate genetic conditions. Then, according to classification schemes relating the quartz CL colour to the genetic environment (Zinkernagel 1978; Ramseyer et al. 1988), the mostly bright bluish and rarely red colours observed suggest "quartz eyes" have a phenocrystic origin (i.e., similar to quartz crystals in volcanic rocks). Likewise the stable

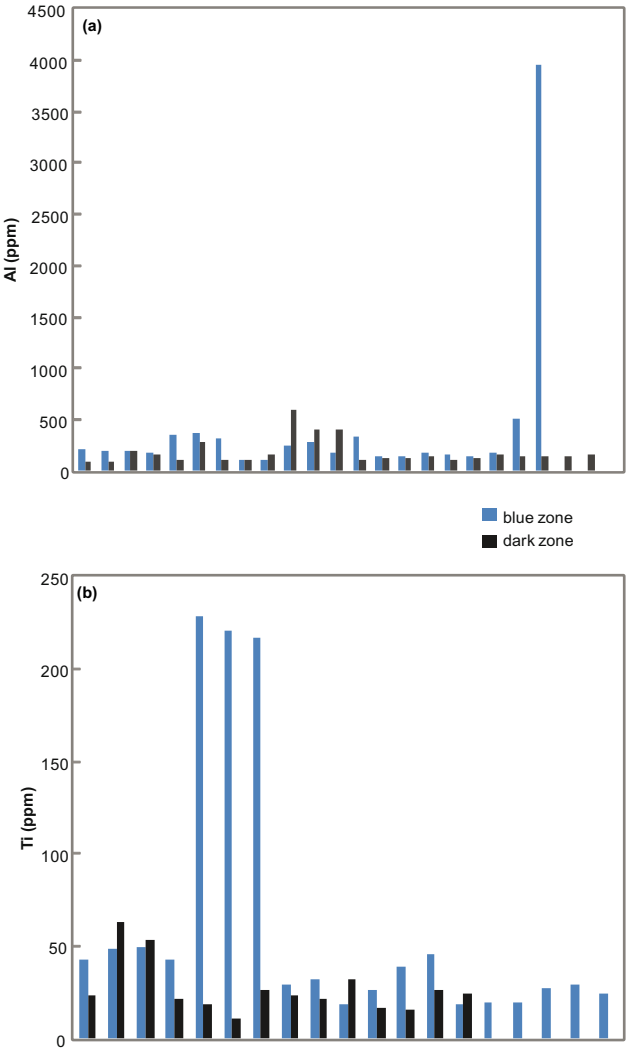

Fig. 10a – Histogram portraying Al distribution in quartz that clearly displays distinct blue rim and dark core**. b** – Histogram of Ti abundances in quartz that clearly displays distinct blue rim and dark core.

luminescence behaviour exhibited by all quartz crystals is indicative of crystallization at higher temperatures, i.e. from a melt, in contrast to transient CL behaviour of quartz formed from relatively low temperature hydrothermal fluids (Götze et al. 2001). If quartz with brown or red CL response is typical of quartz from metamorphic rocks (Zinkernagel 1978; Ramseyer et al. 1988; Boggs et al. 2002), the reddish brown luminescent fluid migration trails observed suggest that some "quartz eyes" underwent retrograde metamorphic fluid reaction. But the reddish-brown and reddish CL colours can also be explained by lattice defects induced by twinning, mechanical deformation, or rapid growth (Ramseyer et al. 1988).

Because of overlap in the CL colour ranges between volcanic, plutonic, metamorphic, and hydrothermal quartz, identification of quartz provenance on the basis of CL colour alone is ambiguous. Regardless, the CL intensity had been recognized to increase proportional to temperature of quartz formation (Rusk et al. 2006). This indicates that cathodoluminescence variability of "quartz eyes" from the NFR Freegold project may reflect temperature fluctuation (probably related to different thermal events) recorded by quartz crystals during their growth.

The trace-element composition of quartz is also known to depend on many parameters, including the following most important: (i) the chemical composition of the quartz-forming environment, (ii) temperature, (iii) pH, (iv) oxygen fugacity and (v) growth rate (Pagel et al. 2000; Götze et al. 2001). Notably, the Ti content is dominantly controlled by temperature (Ti in quartz geothermometer, TITANiQ of Wark et al. 2004, 2006), if Ti phases are present. The temperatures of crystallization and/or reequilibration obtained using the TITANiQ geothermometer, in accordance with the calibration of Wark and Watson (2006), and assuming $^{a}TiO_2 = 1$ are recorded in Tab. 2. Such an $^{a}TiO_2$ is justified by the fact that most of silicic quartz-bearing magmas are relatively Ti-rich, and have at least one phase in which Ti is a stoichiometric component, such as ilmenite or titanite. Even if the system is rutile absent, assuming $^{a}TiO_2 = 1$ will provide a minimum temperature of equilibration, with underestimation of no more than 15 °C (see Wark and Watson 2006). The Ti-poor dark cores as expected recorded lower temperatures (mostly < 600 °C) compared to the Ti-rich blue zones (up to 860 °C). This suggests either overgrowth of magmatic blue zones on xenocrystic dark cores, or a temperature increase assuming equilibrium crystallization and uniformity of Ti activity, and a non-xenocrystic core. In fact, textural phenomena displayed by investigated quartz, such as anhedral, corroded shapes, reaction rims (see Fig. 3f), and magmatic overgrowths are distinct disequilibrium features typical of xenocrysts (see Clarke 2007). Likewise, Bineli Betsi and Lentz (in print) argued for a significant assimilation of crustal rocks during the emplacement of dykes hosting "quartz eyes", suggesting that the latter can possibly represent products of incomplete assimilation (xenocrysts). In addition, oscillatory-zoned crystals (as observed in Fig. 6) exhibit a dark Al-rich and Ti-poor core, whereas the outer shells are brighter and Ti-rich and the outermost shell is dark and Ti-poor as well. This pattern is consistent with quartz overgrowth on a xenocrystic core, consecutively followed by cooling and a crystal fractionation trend leading to the precipitation of low-temperature and Ti-poor quartz at the edge. Furthermore, $\delta^{18}O$ (SMOW) oxygen isotope compositions from separated quartz from Nucleus–Revenue are between 8.9 and 10.1 ‰, suggesting that the magma was derived from, or significantly contaminated by, metasedimentary material. *In situ* oxygen isotope measurements (by the means of SIMS, for example) of

Tab. 2 EPMA element concentration data for quartz eyes from numerous mineralized areas across the NFR Freegold Mountain

	Analyte	Na	Al	SiO_2	K	Ca	Ti	Fe	Mn	Ge	Total oxides	CL color	T	Host	Commodities	Location
	Units	ppm	ppm	wt.%	ppm	ppm	ppm	ppm	ppm	ppm	wt.%		°C	composition		
EPMA spot number	Quartz zone															
TB038, circle 1, grain 1																
1	core	<25	112	100.01	11	<12	29	<57	<10	<66	100.04	blue	617.6	andesitic	Mo–Cu ± W	Nucleus
2	core	31	112	100.01	<8	<12	32	<57	<10	<66	100.04	blue	626.7			
3	rim	49	108	100.01	20	100	23	<57	<10	<66	100.06	gray	596.9			
4	rim	<25	126	100.01	18	14	21	<57	<10	<66	100.05	gray	589.0			
5	rim	<25	246	100.01	<8	57	19	175	<10	<66	100.09	blue	580.5			
6	rim	36	277	100.01	29	81	26	243	<10	<66	100.12	blue	607.7			
7	core	31	105	100.01	12	<12	21	<57	<10	<66	100.04	gray	589.0			
8	core	25	120	100.01	11	<12	19	<57	<10	<66	100.04	gray	580.5			
9	core	39	123	100.01	20	16	11	65	<10	<66	100.06	gray	536.9			
10	core	38	138	100.01	22	19	26	98	<10	<66	100.07	gray	607.7			
11	rim	37	173	100.01	26	42	39	276	<10	<66	100.10	blue	645.5			
12	rim	128	338	100.01	50	84	46	525	<10	<66	100.19	blue	661.9			
46	rim	208	594	100.01	55	88	63	265	<10	<66	100.22	blue	694.7			
47	rim	46	410	100.01	21	75	53	232	<10	<66	100.15	blue	676.4			
TB085B, circle 2																
13	rim	52	89	100.01	40	14	13	<57	<10	<66	100.05	gray	549.8			
14	rim	<25	126	100.01	30	16	<13	<57	<10	<66	100.04	gray				
TB085B, circle 1																
15	rim	<25	150	100.01	27	<12	<13	<57	<10	<66	100.05	blue				
16	rim	18	138	100.01	14	<12	19	<57	<10	<66	100.05	blue	580.5			
17	core	<25	114	100.01	3	<12	<13	<57	<10	<66	100.04	gray				
18	core	30	167	100.01	17	<12	21	<57	<10	<66	100.05	gray	589.0	rhyolitic	Au–Sb	Emmon Hill
19	rim	43	176	100.01	37	18	20	<57	<10	<66	100.07	blue	584.8			
20	rim	40	163	100.01	36	25	20	<57	<10	<66	100.07	blue	584.8			
21	core	<25	284	100.01	37	120	<13	<57	<10	<66	100.09	gray				
22	core	<25	105	100.01	16	6	<13	<57	<10	<66	100.04	gray				
48	groundmass	<25	55	100.01	21	37	<13	<57	<10	<66	100.03	red				
49	groundmass	<25	97	100.01	17	46	<13	<57	<10	<66	100.04	red				
PM3, circle 1																
23		<25	86	100.01	16	84	<13	<57	<10	<66	100.05	gray-blue				
24		<25	107	100.01	21	99	<13	<57	<10	<66	100.05	gray-blue				
25	fracture	71	2027	100.01	172	725	<13	1505	<10	<66	100.72	red		andesitic	Au–Fe–Cu	Goldstar
26	fracture	117	980	100.01	164	449	<13	1213	<10	<66	100.45	red				
250	fracture	<25	498	100.01	89	212	67	361	<10	<66	100.20	red	701.4			
260	fracture	<25	321	100.01	82	153	28	219	<10	<66	100.14	red	614.4			
TB 460, circle 2																
27	edge	57	116	100.01	35	89	21	244	<10	<66	100.09	dark	589.0			
28	edge	58	122	100.01	29	121	30	322	<10	<66	100.11	dark	620.7			
29	core	<25	<15	100.01	4	14	<13	<57	<10	<66	100.02	gray				
30	core	<25	<15	100.01	<8	<12	<13	<57	<10	<66	100.02	gray				
31	core	29	72	100.01	17	<12	30	<57	<10	<66	100.04	gray	620.7			
32	core	<25	64	100.01	11	<12	19	<57	<10	<66	100.03	gray	580.5	andesitic	unknown	Highway
33	rim	11	101	100.01	14	24	30	82	<10	<66	100.05	blue	620.7			
34	rim	<25	94	100.01	12	29	45	79	<10	<66	100.05	blue	659.7			
35	rim	56	71	100.01	31	17	22	<57	<10	<66	100.05	blue	593.0			
36	rim	34	75	100.01	23	13	30	<57	<10	<66	100.05	blue	620.7			
50	thin rim	83	190	100.01	59	128	124	371	<10	<66	100.15	blue	773.8			
51	thin rim	149	448	100.01	81	403	180	834	<10	<66	100.32	blue	823.2			

Tab 2 continued

	Analyte	Na	Al	SiO_2	K	Ca	Ti	Fe	Mn	Ge	Total oxides	CL color	T	Host composition	Commodities	Location
	Units	ppm	ppm	wt.%	ppm	ppm	ppm	ppm	ppm	ppm	wt.%		°C			
EPMA spot number	Quartz zone															
							TB 383, circle 1									
37	core	<25	119	100.01	9	14	<13	89	<10	<66	100.05	bluish				
38	core	<25	124	100.01	<8	<12	<13	78	<10	<66	100.05	bluish				
39	core	<25	131	100.01	<8	13	19	81	<10	<66	100.05	bluish	580.5			
40	fracture	64	422	100.01	10	54	<13	251	<10	<66	100.14	red				
41	fracture	<25	160	100.01	<8	20	<13	158	<10	<66	100.07	red		andesitic	Mo–Cu ± W	Stoddart
42	fracture	<25	174	100.01	<8	28	<13	132	<10	<66	100.07	red				
43	rim	433	1790	100.01	323	965	1138	2301	25	<66	101.07	red	1156.5			
44	rim	219	972	100.01	93	281	392	1059	<10	<66	100.48	red	942.8			
45	rim	261	6311	100.01	841	2750	1605	635	<10	<66	102.08	red	1242.4			
							TB 189, circle 1									
52	rim	<25	144	100.01	58	18	<13	<57	<10	<66	100.05	gray				
53	rim	<25	133	100.01	34	24	14	<57	<10	<66	100.05	gray	555.6			
54	rim	<25	390	100.01	135	583	<13	<57	<10	<66	100.19	blue				
55	rim	<25	144	100.01	55	14	28	<57	<10	<66	100.05	blue	614.4	rhyolitic	Au–Bi–As–Cu	Nucleus
56	rim	<25	128	100.01	35	<12	36	<57	<10	<66	100.05	blue	637.8			
57	core	<25	207	100.01	40	14	<13	<57	<10	<66	100.06	gray				
58	core	<25	85	100.01	11	<12	<13	<57	<10	<66	100.03	gray				
							TB 407, circle1									
59	rim	61	159	100.01	19	18	<13	85	<10	<66	100.07	gray				
60	rim	<25	202	100.01	<8	17	<13	86	<10	<66	100.06	gray				
61	rim	<25	158	100.01	16	20	<13	92	<10	<66	100.06	gray				
62	core	<25	144	100.01	<8	18	<13	<57	<10	<66	100.04	blue		rhyolitic	Au–Bi–As–Cu	Nucleus
63	core	<25	130	100.01	<8	13	16	<57	<10	<66	100.04	blue	566.3			
64	core	<25	110	100.01	3	<12	14	<57	<10	<66	100.04	blue	555.6			
							TB 323, circle 3									
65	core	<25	203	100.01	<8	<12	<13	<57	<10	<66	100.05	gray-bluish				
66	core	<25	156	100.01	<8	13	14	<57	<10	<66	100.05	gray-bluish	555.6			
67	core	<25	227	100.01	25	14	<13	<57	<10	<66	100.06	gray				
68	core	<25	157	100.01	9	<12	13	<57	<10	<66	100.05	gray	549.8			
69	rim	<25	202	100.01	23	<12	<13	<57	<10	<66	100.06	gray-bluish				
70	rim	<25	181	100.01	13	19	<13	<57	<10	69	100.06	gray-bluish				
71	rim	<25	188	100.01	53	<12	18	<57	<10	<66	100.07	gray	576.0			
72	rim	<25	183	100.01	55	<12	17	<57	<10	<66	100.07	gray	571.3			
94	rim	25	1518	100.01	326	41	34	<57	<10	<66	100.36	blue	632.4			
95	rim	<25	200	100.01	103	<12	30	<57	<10	<66	100.07	blue	620.7			
73	core	<25	218	100.01	<8	17	<13	<57	<10	<66	100.06	dark		rhyolitic	Au–Bi–As–Cu	Nucleus
74	core	<25	131	100.01	10	<12	<13	<57	<10	<66	100.04	dark				
75	fracture	<25	66	100.01	<8	<12	<13	<57	<10	<66	100.03	red				
76	fracture	<25	58	100.01	<8	<12	<13	<57	<10	<66	100.03	red				
77	core	<25	112	100.01	<8	<12	36	<57	<10	71	100.05	gray	637.8			
78	core	<25	122	100.01	13	17	<13	<57	<10	<66	100.04	gray				
79	rim	<25	277	100.01	62	65	<13	98	<10	<66	100.09	gray				
80	rim	<25	163	100.01	51	59	<13	<57	<10	<66	100.06	gray				
81	rim	<25	436	100.01	73	54	62	660	11	<66	100.21	red	693.0			
82	rim	<25	379	100.01	33	46	113	584	<10	<66	100.19	red	762.2			

Tab 2 continued

	Analytes	Na	Al	SiO_2	K	Ca	Ti	Fe	Mn	Ge	Total oxides	CL color	T	Host composition	Commodities	Location
	Units	ppm	ppm	wt.%	ppm	ppm	ppm	ppm	ppm	ppm	wt.%		°C			
EPMA spot number	Quartz zone															
							TB 174A, circle 1									
83	fracture	<25	72	100.01	43	14	<13	57	<10	<66	100.04	red				
84	fracture	<25	71	100.01	73	<12	<13	70	<10	<66	100.05	red				
85	fracture	39	172	100.01	132	<12	<13	<57	<10	<66	100.07	red				
86	fracture	<25	137	100.01	117	<12	<13	<57	<10	<66	100.06	red				
87	fracture	<25	65	100.01	91	<12	<13	<57	<10	<66	100.04	red				
88		<25	101	100.01	39	39	<13	<57	<10	<66	100.05	blue		rhyolitic	Au–Cu	Revenue
89		<25	135	100.01	95	29	29	162	<10	<66	100.08	blue	617.6			
90		<25	107	100.01	36	25	<13	<57	<10	<66	100.04	blue				
91		<25	85	100.01	31	16	<13	<57	<10	<66	100.04	brown				
92		<25	71	100.01	23	28	<13	<57	<10	<66	100.04	brown				
93		<25	76	100.01	27	46	<13	<57	<10	<66	100.04	brown				
							TB 085B, circle 1									
96	rim	71	138	100.01	<8	<12	<13	<57	<10	<66	100.05	blue				
97	core	<25	101	100.01	<8	<12	<13	<57	<10	<66	100.03	gray				
							TB 085B, circle 3							rhyolitic	Au–Sb	Emmon Hill
98	core	<25	186	100.01	<8	<12	27	<57	<10	<66	100.06	blue	611.1			
99	rim	<25	168	100.01	<8	<12	<13	<57	<10	<66	100.05	gray				
							TB 218, circle 1									
100	core	<25	195	100.01	<8	<12	23	<57	<10	<66	100.06	gray	596.9			
101	rim	<25	511	100.01	<8	3440	29	575	<10	<66	100.67	blue	617.6			
							TB 218, circle 2							trachytic	base–metal–Au–Ag	Tinta Hill
102	core	<25	94	100.01	<8	<12	<13	<57	<10	72	100.04	gray				
103	core	<25	95	100.01	<8	<12	<13	<57	<10	<66	100.04	gray				
104	rim	<25	3952	100.01	37	192	24	8839	92	<66	101.95	blue	600.6			
							TB 174 circle 1									
105	fracture	<25	36	100.01	<8	<12	<13	<57	<10	<66	100.03	red		trachy-dacitic	Au–Cu	Revenue
106		<25	149	100.01	26	<12	<13	<57	<10	<66	100.05	blue				
							TB 407, circle 1									
107	rim	<25	107	100.01	<8	<12	**<13**	<57	<10	**<66**	100.04	blue		rhyolitic		
108	core	<25	107	100.01	<8	<12	<13	<57	<10	66	100.04	gray				
							TB 189								Au–Bi–Cu–AS	Nucleus
109	core	<25	92	100.01	<8	<12	<13	<57	<10	<66	100.04	gray		rhyolitic		
110	rim	<25	214	100.01	<8	57	<13	346	<10	<66	100.11	blue				

both the core and the rim of quartz may better constrain the origin of the dark Ti-depleted cores.

On the other hand, an increase in crystallization temperature is possible as well. Such a pattern had been observed in quartz phenocrysts from the Bishop Tuff, where dark and Ti-depleted cores formed at lower temperatures, relative to the Ti-enriched bright rims (Wark et al. 2004). However, an increase in temperature with time is inconsistent with either hydrothermal or magmatic hydrothermal transition environments, designated as loci of "quartz eyes" formation in numerous porphyry copper deposits (Harris et al. 2003, 2004; Vasyuka et al. 2008). Instead, such a pattern points to an evolution within a magma chamber, and it is reasonable to postulate a phenocrystic origin to some of the "quartz eyes" investigated.

In addition to the "quartz eye" phenocrysts, and possibly xenocrysts and xenocrystic cores, there are also broken "quartz eyes" (phenoclasts) as above described. Fragmentation of crystals in igneous processes has been assigned to numerous factors, including mostly: (i) the pre-eruptive decrepitation of melt inclusions occurring either upon decompression or magma overheating, (ii) the

Tab 2 continued

	Analytes	Na	Al	SiO_2	K	Ca	Ti	Fe	Mn	Ge	Total oxides	CL color	T	Host composition	Commodities	Location
	Units	ppm	ppm	wt.%	ppm	ppm	ppm	ppm	ppm	ppm	wt.%		°C			
EPMA spot number	Quartz zone															
TB 323																
115	core	<25	179	100.01	<8	<12	<13	<57	<10	<66	100.05	gray				
129	core	<25	738	100.01	<8	<12	<13	<57	<10	<66	100.15	gray				
130	core	<25	163	100.01	<8	<12	<13	<57	<10	<66	100.05	gray				
131	core	<25	177	100.01	<8	<12	15	<57	<10	<66	100.05	gray	561.1			
116	rim	<25	241	100.01	<8	<12	<13	<57	<10	<66	100.06	gray-bluish				
133	rim	<25	207	100.01	<8	<12	23	<57	<10	<66	100.06	gray-bluish				
134	rim	<25	169	100.01	<8	<12	18	<57	<10	<66	100.05	gray-bluish	596.9			
135	rim	<25	191	100.01	<8	<12	13	<57	<10	<66	100.05	gray-bluish	576.0	rhyolitic	Au–Bi–Cu–AS	Nucleus
118	edge	<25	438	100.01	11	<12	<13	<57	<10	<66	100.1	gray-bluish	549.8			
139	edge	<25	303	100.01	11	<12	<13	<57	<10	<66	100.08	gray-bluish				
140	edge	<25	184	100.01	<8	<12	<13	<57	<10	<66	100.05	gray-bluish				
141	edge	<25	270	100.01	8	<12	<13	<57	<10	<66	100.07	gray-bluish				
117	rim	<25	318	100.01	<8	<12	<13	<57	<10	<66	100.07	blue-grayish				
136	rim	<25	211	100.01	<8	<12	14	<57	<10	<66	100.06	blue-grayish	555.6			
137	rim	<25	184	100.01	<8	<12	18	<57	<10	<66	100.05	blue-grayish	576.0			
138	rim	<25	179	100.01	<8	<12	15	<57	<10	<66	100.05	blue-grayish	561.1			
TB 038, circle 1, grain 2																
111	rim	<25	210	100.01	<8	<12	43	84	<10	<66	100.07	blue	655.1			
123	rim	<25	187	100.01	<8	<12	49	129	<10	<66	100.08	blue	668.3			
124	rim	<25	188	100.01	<8	<12	50	70	<10	<66	100.07	blue	670.4			
125	rim	<25	182	100.01	<8	<12	43	<57	<10	<66	100.06	blue	655.1			
112	core	<25	149	100.01	<8	<12	17	<57	<10	<66	100.04	gray	571.3			
126	core	<25	151	100.01	<8	<12	16	<57	<10	<66	100.05	gray	566.3			
127	core	<25	145	100.01	<8	<12	26	<57	<10	<66	100.04	gray	607.7	andesitic	Mo–Cu ± W	Stoddart
128	core	<25	168	100.01	<8	<12	24	<57	<10	<66	100.05	gray	600.6			
TB 038, circle 2																
113	core	<25	162	100.01	<8	<12	32	<57	<10	<66	100.05	gray	626.7			
114	rim	<25	351	100.01	17	36	229	208	<10	<66	100.15	blue	857.6			
142	rim	<25	377	100.01	15	47	221	183	<10	<66	100.16	blue	852.4			
143	rim	<25	309	100.01	<8	99	217	228	<10	<66	100.15	blue	849.7			
TB 460, circle 2																
119	rim	<25	114	100.01	<8	<12	40	154	<10	<66	100.06	bright blue	648.0			
123	rim	<25	117	100.01	<8	<12	35	87	<10	<66	100.06	bright blue	635.1			
120	edge	<25	120	100.01	<8	60	31	444	<10	<66	100.11	dark bluish	623.7	andesitic	unknown	Highway
121	rim	<25	128	100.01	<8	<12	36	108	<10	<66	100.06	dark bluish	637.8			
122	core	<25	98	100.01	<8	<12	30	<57	<10	<66	100.04	dark bluish	620.7			

Temperatures were calculated using the calibration from Wark and Watson (2006)

syn-eruptive shockwave and mutual impact fragmentation and (iii) the pre- to post-eruptive disaggregation of glomerophyric clots (Best and Christiansen 1997; Bindeman 2005). Fragmented quartz crystals in dykes across the Freegold Mountain commonly display no more than three fragments (see Fig. 3c). This is consistent with melt inclusions decrepitation-related fragmentation, rather than syn-eruptive mutual impact breakage that is more likely to yield a high (at least 10) number of fragments (Bindeman 2005). This does not preclude a syn-eruptive fragmentation, i.e., analogous to tuffisite, followed by later devitrification of the glassy groundmass. The presence of abundant spherulites of chlorite (probably after feldspar) (see Fig. 3a) in sample TB 085 from Emmon

Hill may be indicative of high-temperature glass devitrification (see Lofgren 1971).

Quartz textures as revealed by ChromaSEM-CL also show an overprint of the phenocrysts by reddish-brown quartz that is typically Al-depleted (36 ppm) relative to other quartz growth zones (91 < Al < 3 953 ppm) and recorded Ti, Fe, and Ca contents lower than the detection limit. Given that even early experimental studies also indicated that the amount of Al incorporated into quartz is affected by the temperature (see Dennen et al. 1970), it follows that the reddish-brown quartz is probably of lower temperature origin. Therefore, the weakly luminescent and Al- and Ti-poor fluid migration trails are better interpreted as the result of interaction of deuteric fluids with quartz phenocrysts, phenoclasts, and xenocrysts. Such dull luminescent trails are common feature of quartz from subvolcanic environments and have been reported in numerous porphyry systems (see Rusk et al. 2005; Müller et al. 2010). However, the origin of some high-temperature and trace-element-rich red quartz (spots 81 and 82, Fig. 7d and Tab. 2) is uncertain.

6.3. Implications for dyke emplacement and ore genesis

Based on the assumption that the abundance of trace elements (including Ti) in quartz is mainly controlled by the concentration of the elements in the melt, and assuming that the cores (overgrown by blue rim) are not xenocrystic, the increase in temperature of crystallization could reflect either crystals sinking (settling) into hotter regions of the magma system, or underplating by newly injected hot, more mafic/less fractionated melt, or magma mixing. Considering the small density contrast between quartz crystal and felsic magma (of higher viscosity), crystal settling appears to be an unlikely process. Therefore, underplating and/or magma mixing are the most plausible explanations for elevated temperature of outer shells. Textural evidence such as partial resorption or corrosion likely to occur under changing magmatic conditions further testifies to the magma mixing–mingling processes (see Hibbard 1981; Glazner et al. 1990; Müller et al. 2005). Likewise, the observed crystal fragmentation may be related to the magma mixing as well. In fact, as pointed out by Bindeman (2005), chamber recharge by hotter magmas may result in mass decrepitation of melt inclusions and crystal fragmentation in the colder magma. Additional disequilibrium features such as amphibole corona mantling ocellar quartz (Fig. 3g) point not only to magma mixing/mingling processes, but also to multiple recharge of more mafic magma into the magma chamber of a crystallizing silicic melt. Likewise, "quartz eye" rims from an andesitic host sample display great variability in Ti content, and by association in T of crystallization and/or reequilibration: one crystal recorded between 43 and 50 ppm Ti, corresponding to 655–670 °C, and the second between 217 and 229 ppm Ti, consistent with 850–858 °C (Tab. 2). This discrepancy in the composition of the outer shells of "quartz eyes" crystals implies multiple phases of magma mixing, and by inference a discontinuous input of magma. The multiple recharge of magma suggests a dyke emplacement controlled by step-wise accumulation of individual magma batches (see Maaløe 1987; Bons et al. 2001).

Discontinuous magma input is of significant importance in ore genesis (see Vigneresse 2007). A mafic magma intruding a cold felsic magma chamber will lead to an elevated temperature variation in the latter. The large temperature variation will significantly affect the oxygen fugacity values of both magmas, and by association coefficients for metal partitioning between mineral and melt, for they are very sensitive to oxygen fugacity. Also, the intrusion of a mafic magma with high fluid solubility into cold felsic magma may result in the sudden exsolution of a fluid phase (see Vigneresse 2007). This fluid exsolution process is similar to the second boiling, i.e., not related to any pressure decrease (see Burnham 1985). However, this does not rule out the adiabatic decompression (due to the rapid magma ascent), which likely took place across the Freegold Mountain area. Such a scenario is supported by not only the fine-grained nature of the groundmass in dykes, but also the presence of deep and sinuous embayments leading to vermicular quartz (Figs 3e–f). Such deep resorption of quartz crystals had been suggested to occur in the presence of both magma and F-rich magmatic hydrothermal fluids, i.e., at the magmatic–hydrothermal transition (see Chang and Meinert 2004).

The significant magma degassing that could have followed magma mixing or decompression, and probably the tuffisitic emplacement of some dykes, is an important factor for ore minerals deposition in hydrothermal systems (see Giggenbach 2003; Giggenbach et al. 2003), that is likely responsible for mineralization throughout the Freegold Mountain area and therefore explains the spatial association of dykes and mineralization.

Furthermore, mixing of felsic and mafic magmas is also likely responsible for some of Au endowment in the Freegold Mountain area. In fact, in Cu– (Au–Mo) and porphyry Au deposits, co-mingling of mafic with silicic magma had been reported to increase the Au budget of the deposits (e.g., at Bingham, Keith et al. 1998; Tarkian and Stribrny 1999; Hattori and Keith 2001; Maughan et al. 2002). Quartz textures also indicate that the dykes from the study area probably cooled rapidly. This is supported by the presence of dendritic quartz that may be a normal result of crystallization under conditions of moderately high cooling rate (see Swanson and Fenn 1986; MacLellan and Trembath 1991). The cooling rate

and concurrent exhumation rate of magmatic bodies are regarded as important factors associated to genesis and grade of mineralization, and a positive correlation between metal grade and cooling rate during hypogene ore formation has been reported (McInnes et al. 2005). Therefore the interpreted elevated cooling rate assigned to dykes within the Freegold Mountain region seems to have somehow controlled the grade of the mineralization.

7. Conclusions

The results obtained in the course of this study indicate that:

1. The ChromaSEM-CL colours of quartz are related to its trace-element abundances, with dark growth zones typically poor in Ti compared with bright blue ones.
2. Titanium is regarded as the cathodoluminescence activator for there is a clear correlation between the Ti abundance and the CL response.
3. In all colour-zoned quartz crystals, the Ti-poor dark cores recorded lower temperatures, compared to the relatively Ti-rich bright blue overgrowths.
4. "Quartz eyes" in porphyritic dykes from Freegold Mountain represent phenocrysts and phenoclasts, which in places are overprinted by low-temperature hydrothermal quartz. However, some dark cores represent restite from incomplete dissolution of source region materials and/or xenocrysts of wall rocks traversed during magma ascent. Therefore, further investigations are needed to clearly decipher the nature of some of the darker cores.
5. Magma mixing was a major process in the evolution of porphyritic dykes in the Freegold Mountain and multiple magma mixing phases are likely to have occurred. These dykes were also subjected to a high cooling rate and decompression of the magmatic system, accompanying their ascent and emplacement.
6. Volatile exsolution that could have resulted from both magma mixing and decompression may have been of significant importance for ore mineral formation.

Acknowledgements. The authors are grateful to the Yukon Geological Survey (YGS) for the funding allocated to this study, and a NSERC Discovery grant to David Lentz. They also acknowledge Northern Freegold Resources, owner of the NFR Freegold Mountain project, for financial and logistic support and allowing access to the property. We thank Douglas Hall for his assistance with the SEM-CL and EPMA. The two reviewers, Axel Müller and Eric Christiansen, are thanked for their suggestions and comments, which undoubtedly improved this manuscript.

References

Best MG, Christiansen EH (1997) Origin of broken phenocrysts in ash-flow tuffs. Geol Soc Am Bull 109: 63–73

Bindeman IN (2005) Fragmentation phenomena in populations of magmatic crystals. Amer Miner 90: 1801–1815

Bineli Betsi T, Bennett V (2010) New U–Pb age constraints at Freegold Mountain: evidence for multiple phases of polymetallic mid- to Late Cretaceous mineralization. In: Emond DS, Lewis LL, Weston LH Colpron MN, Nelson JL (eds) Yukon Exploration and Geology 2009. Yukon Geological Survey, Whitehorse, pp 57–84

Bineli Betsi T, Lentz DR (2009) Petrogenesis of dykes related to Cu–Au & base-metal Au–Ag occurrences, Mt. Freegold area, Dawson Range, Yukon Territory, Canada. In: Lentz DR, Thorne KG, Beal, K–L (eds) Proceedings of the 24th International Applied Geochemistry Symposium. Fredericton, Canada, pp 115–118

Bineli Betsi T, Lentz DR (in press) Petrochemistry of subvolcanic dyke swarms associated with the Golden Revenue Au–Cu and the Stoddart Mo–Cu ± W mineralizations (Dawson Range, Yukon Territory, Canada) and implications for ore genesis. Ore Geol Rev, accepted

Boggs S Jr, Kwon YI, Goles GG, Rusk BG, Krinsley D, Seyedolali A (2002) Is quartz cathodoluminescence color a reliable provenance tool? A quantitative examination. J Sed Res 72: 408–415

Bons PD, Dougherty-Page J, Elburg MA (2001) Stepwise accumulation and ascent of magmas. J Metamorph Geol 19: 627–633

Breiter K, Müller A (2009) Evolution of rare-metal granitic magmas documented by quartz chemistry. Eur J Mineral 21: 335–346

Burnham CW (1985) Energy release in subvolcanic environments: implications for breccia formation. Econ Geol 80: 1515–1522

Chang Z, Meinert LD (2004). The magmatic–hydrothermal transition – evidence from quartz phenocryst textures and endoskarn abundance in Cu–Zn skarns at the Empire Mine, Idaho, USA. Chem Geol 210: 149–171

Clarke DB (2007) Assimilation of xenocrysts in granitic magmas: principles, processes, proxies and problems. Canad Mineral 45: 5–30

Colpron MN, Nelson JL, Murphy DC (2006) A tectonostratigraphic framework for the Pericratonic terranes of the northern Canadian Cordillera. In: Colpron MN, Nelson JL (eds) Paleozoic Evolution and Metallogeny of Pericratonic Terranes at the Ancient Pacific Margin of North America, Canadian and Alaskan Cordillera. Geological Association of Canada 45: pp 1–23

Demars C, Pagel M, Deloule E, Blanc P (1996) Cathodoluminescence of quartz from sandstone: interpretation of the UV range by determination of trace element distribu-

tion and fluid-inclusion P–T–X properties in authigenic quartz. Amer Miner 81: 891–901

Dennen WH (1967) Trace elements in quartz as indicator of provenance. Geol Soc Am Bull 78: 125–130

Dennen WH, Blackburn WH, Quesada A (1970) Aluminum in quartz as a geothermometer. Contrib Mineral Petrol 27: 332–342

Evans JEL (1944) Porphyry of the Porcupine district, Ontario. Geol Soc Am Bull 55: 1115–1142

Fisher M, Roeller K, Kuester M, Stoeckhert B, McConnell VS (2003) Open fissure mineralization at 2600 m depth in Long Valley Exploration Well (California); insight into the history of the hydrothermal system. J Volcanol Geotherm Res 127: 347–363

Fournier RO (1999) Hydrothermal processes related to movement of fluid from plastic into brittle rock in the magmatic–epithermal environment. Econ Geol 94: 1193–1211

Giggenbach WF (2003) Magma degassing and mineral deposition in hydrothermal systems along convergent plate boundaries. In: Stuart FS, Ian G (eds) Volcanic, Geothermal, and Ore Forming Fluids: Rulers and Witnesses of Processes Within the Earth. Soc Econ Geol Spec Publication 10: pp 1–18

Giggenbach WF, Shinohara H, Kusakabe M, Ohba T (2003) Formation of acid volcanic brines through interaction of magmatic gases, seawater, and rock within the White island volcanic-hydrothermal system, New Zealand. In: Stuart FS, Ian G (eds) Volcanic, Geothermal, and Ore Forming Fluids: Rulers and Witnesses of Processes Within the Earth. Soc Econ Geol Spec Publication 10: pp 19–40

Glazner AF, Ussler W, Mathis AC (1990) Interpretation of plagioclase texture in volcanic rocks. EOS (Transactions of the American Geophysical Union) 71: 1678

Götze JM (2002) Potential of cathodoluminescence (CL) microscopy and spectroscopy for the analysis of minerals and materials. Anal Bioanal Chem 374: 703–708

Götze JM, Plötze M (1997) Investigation of trace-element distribution in detrital quartz by Electron Paramagnetic Resonance (EPR). Eur J Mineral 9: 529–537

Götze JM, Plötze M, Habermann D (2001) Origin, spectral characteristics and practical applications of the cathodoluminescence (CL) of quartz – a review. Mineral Petrol 71: 225–250

Götze JM, Plötze M, Graupner T, Hallbauer DK, Bray CJ (2004) Trace element incorporation into quartz: a combined study by ICP-MS, electron spin resonance, cathodoluminescence, capillary ion analysis, and gas chromatography. Geochim Cosmochim Acta 68: 3741–3759

Grant PR, White SH (1978) Cathodoluminescence and microstructure of quartz overgrowths on quartz. In: Johari O (ed) Scanning Electron Microscopy. Scanning Electron Microscopy, Chicago, pp 789–794

Hattori KH, Keith JD (2001) Contribution of mafic melt to porphyry copper mineralization: evidence from Mount Pinatubo, Philippines, and Bingham Canyon, Utah, USA. Miner Depos 36: 799–806

Harris AC, Kametsky VS, White NC (2003) Immiscible magmatic volatiles in the Bajo de la Alumbrera Cu–Au deposit. Melt and fluid record in quartz eye. In: Eliopoulos D et al. (eds) Mineral Exploration and Sustainable Development. Society for Geology Applied to Mineral Deposits (SGA), the 7th Biennial Meeting, Athens, Greece, pp 275–278

Harris AC, Kamenetsky VS, White NC (2004) The magmatic–hydrothermal transition: volatile separation in silicic rocks at Bajo de la Alumbrera porphyry Cu–Au deposit, NW Argentina. In: Blevin P, Champion D (eds) The Ishihara Symposium: Granite and Associated Metallogenesis, pp 69–74

Hayward CL (1998) Cathodoluminescence of ore and gangue minerals and its application in the minerals industry. In: Cabri J, Vaughan DJ (eds) Modern Approaches to Ore and Environmental Mineralogy. Mineralogical Association of Canada Short Course Series 27: pp 269–325

Hibbard MJ (1981) The magma mixing origin of mantled feldspar. Contrib Mineral Petrol 76: 158–170

Jacamon F, Larsen RB (2009) Trace element evolution of quartz in the charnockitic Kleivan granite, SW-Norway: The Ge/Ti ratio of quartz as an index of igneous differentiation. Lithos 107: 281–291

Keith JD, Christiansen EH, Maughan DT, Waite KA (1998) The role of mafic alkaline magmas in felsic porphyry-Cu and Mo systems. In: Lentz DR (ed) Mineralized Intrusion-Related Skarn Systems. Mineralogical Association of Canada Short Course Series 26: pp 211–243

Kempe U, Götze J, Dandar S, Haberman D (1999) Magmatic and metasomatic processes during formation of the Nb–Zr–REE deposits from Khaldzan Buregte (Mongolian Altai): indication from a combined CL–SEM study. Mineral Mag 63: 165–167

Landtwing MR, Pettke T (2005) Relationship between SEM-cathodoluminescence response and trace element composition of hydrothermal vein quartz. Amer Miner 90: 122–131

Lofgren G (1971) Experimentally produced devitrification textures in natural rhyolitic glass. Geol Soc Am Bull 82: 111–124

Lofgren G. (1980) Experimental studies on the dynamic crystallization of silicate melt. In: Hargraves RB (ed) Physic of Magmatic Processes. Princeton University Press, Princeton, New Jersey, pp 487–551

Maaløe S. (1987) The generation and shape of feeder dykes from mantle sources. Contrib Mineral Petrol 96: 47–55

Maclellan HE, Trembath L (1991) The role of quartz crystallization in the development and preservation of

igneous texture in granitic rocks: experimental evidence at 1 kbar. Amer Miner 76: 1291–1305

Marshall DJ (1988) Cathodoluminescence of Geological Materials. Unwin Hyman Ltd, Boston, Massachusetts, pp 1–146

Maughan DT, Keith JD, Christiansen EH, Pulsipher T, Hattori K, Evans NJ (2002) Contributions from mafic alkaline magmas to the Bingham porphyry Cu–Au–Mo deposit, Utah, USA. Miner Depos 37: 14–37

McInnes, BIA, Goodfellow WD, Crocket JH, McNutt RH (1988) Geology, geochemistry and geochronology of subvolcanic intrusions associated with gold deposits at Freegold Mountain, Dawson Range, Yukon. Geological Survey of Canada, Current Research 88-1E, pp 137–151

McInnes BIA, Evans NJ, Fu FQ, Garwin S, Belousova E, Griffin WL, Bertens A, Sukarna D, Permanadewi S, Andrew RS, Deckart K (2005) Thermal history analysis of selected Chilean, Indonesian and Iranian porphyry Cu–Mo–Au deposits. In: Porter TM (ed) Super Porphyry Copper and Gold Deposits. A Global Perspective. PGC publishing, Adelaide, pp 1–16

Monecke T, Kempe U, Götze J (2002) Genetic significance of the trace element content in metamorphic and hydrothermal quartz: a reconnaissance study: Earth Plan Sci Lett 202: 709–724

Müller A, Koch-Müller M (2009) Hydrogen speciation and trace element contents of igneous, hydrothermal and metamorphic quartz from Norway. Mineral Mag 73: 569–583

Müller A, Lennox P, Trzebski R (2002a) Cathodoluminescence and micro-structural evidence for crystallization and deformation processes of granites in the Eastern Lachlan Fold Belt (SE Australia). Contrib Mineral Petrol 143: 510–524

Müller A, Kronz A, Breiter K (2002b) Trace elements and growth patterns in quartz; a fingerprint of the evolution of the subvolcanic Podlesí granite system (Krušné hory Mts., Czech Republic). In: Breiter K (ed) Selected Papers Presented on International Workshop "Phosphorus- and Fluorine-rich Fractionated Granites". Bull Czech Geol Surv 77: 135–145

Müller A, Wiedenbeck M, van den Kerkhof AM, Kronz A, Simon K (2003a) Trace elements in quartz – a combined electron microprobe, secondary ion mass spectrometry, laser-ablation ICP-MS, and cathodoluminescence study. Eur J Mineral 15: 747–763

Müller A, René M, Behr HJ, Kronz A (2003b) Trace elements and cathodoluminescence of igneous quartz in topaz granites from the Hub Stock (Slavkovský les Mts., Czech Republic). Mineral Petrol 79: 167–191

Müller A, Breiter K, Seltmann R, Pecskay Z (2005) Quartz and feldspar zoning in the eastern Erzgebirge Volcano–plutonic Complex (Germany, Czech Republic): evidence of multiple magma mixing. Lithos 80: 201–227

Müller A, van den Kerkhof AM, Behr HJ, Kronz A, Koch–Müller M (2009) The evolution of late-Hercynian granites and rhyolites documented by quartz – a review. Earth Environ Sci Trans R Soc Edinb 100: 185–204

Müller A, Herrington R, Armstrong R, Seltmann R, Kirwin DJ, Stenina NG, Kronz A (2010) Trace elements and cathodoluminescence of quartz in stockwork veins of Mongolian porphyry-style deposits. Miner Depos 45: 707–727

Pagel M, Barbarin V, Blanc P, Ohnenstetter D (2000) Cathodoluminescence in Geosciences. Springer-Verlag, Berlin, pp 1–514

Penniston-Dorland SC (2001) Illumination of vein quartz textures in a porphyry copper ore deposit using scanned cathodoluminescence: Grasberg Igneous Complex, Irian Jaya, Indonesia. Amer Miner 86: 652–666

Penny B, Eberhardt P, Ramseyer K. Mullis J, Pankrath R (1992) Microdistribution of Al, Li, and Na in alpha-quartz – possible causes and correlation with short-lived cathodoluminescence. Amer Miner 77: 534–544

Ramseyer K, Baumann, J, Matter A, Mullis J (1988) Cathodoluminescence colours of alpha quartz. Mineral Mag 52: 669–677

Ramseyer K, Mullis J (1990) Factors influencing short-lived blue cathodoluminescence of alpha-quartz. Amer Miner 75: 791–800

Robinson BW, Ware NG, Smith DGW (1998) Modern electron-microprobe trace-element analysis in mineralogy. In Cabri J, Vaughan DJ (eds) Modern Approaches to Ore and Environmental Mineralogy. Mineralogical Association of Canada Short Course Series 27: pp 153–180

Roedder E (1979) Origin and significance of magmatic inclusions. Bull Minéral 102: 487–510

Rusk BG, Reed M, Krinsley D, Bignall G, Tsuchiya N (2005) Natural and synthetic quartz growth and dissolution revealed by scanning electron microscope-cathodoluminescence. In: Nakahara M et al. (eds) Proceedings of 14th International Conference on the Properties of Water and Steam. Maruzen Co., Ltd., Kyoto, pp 296–302

Rusk BG, Reed MK, Dilles JH, Kent A JR (2006) Intensity of quartz cathodoluminescence and trace-element content in quartz from the porphyry copper at Butte, Montana. Amer Miner 91: 1300–1312

Smuk KA (1999) Metallogeny of Epithermal Gold and Base Metal Veins of the Southern Dawson Range, Yukon. Unpublished MSc. Thesis, McGill University, Montreal, Québec, pp 1–155

Swanson SE, Fenn PM (1986) Quartz crystallization in igneous rocks. Amer Miner 71: 331–342

Tarkian M, Stribrny B (1999) Platinum-group elements in porphyry copper deposits: a reconnaissance study. Mineral Petrol 65: 161–183

van den Kerkhof AM, Kronz A, Simon K (2001) Trace element redistribution in metamorphic quartz and fluid

inclusion modifications: observations by cathodoluminescence. In: XVI ECROFI, Porto, 2001, Abstracts. Faculdade de Ciências de Porto, Departamento de Geologia, Memoria 7: pp 447–450

Vasyukova OV, Kamenetsky VS, Gömann K (2008) Origin of "quartz eyes" and fluid inclusions in mineralized porphyries. Geochim Cosmochim Acta 72: A978

Vernon RH (1986) Evaluation of the "quartz-eye" hypothesis. Econ Geol 81: 1520–1527

Vigneresse JL (2007) The role of discontinuous magma inputs in felsic magma and ore generation. Ore Geol Rev 30: 181–216

Wark DA, Watson EB (2006) TitaniQ: a titanium-in-quartz geothermometer. Contrib Mineral Petrol 152: 743–754

Wark DA, Anderson AT, Watson EB (2004) Probing Ti in quartz: application of the TITANiQ thermometer to the Bishop Tuff. American Geophysical Union, Spring Meeting 2004, abstract #V34B-04

Wark DA, Watson EB, Spear FS, Cherniak D, Wiebe RA (2006) Titanium in quartz; thermometry, diffusion, and cathodoluminescence. Geological Society of America Northeastern Section, 41st Annual Meeting. Geological Society of America Abstracts with Programs 38: 5

Watt GR, Wright P, Galloway S, McLean C (1997) Cathodoluminescence and trace element zoning in quartz phenocrysts and xenocrysts. Geochim Cosmochim Acta 61: 4337–4348

Wheeler JO, McFeely P (*Compilers*) (1991). Tectonic assemblage map of the Canadian Cordilleran and adjacent parts of the United States of America. Geological Survey of Canada, Map 1712A, scale 1 : 2 000 000.

Williams P, Carmichael A (1987) Evaluation of the "quartz eyes" hypothesis – a discussion. Econ Geol 82: 1081–1082

Zinkernagel U (1978) Cathodoluminescence of Quartz and its Application to Sandstone Petrology. E. Schweizerbart'sche Verlagsbuchlandlung (Naegele u. Obermiller), Stuttgart, pp 1–69